

10-11-2024

Long-Distance Photon-Mediated and Short-Distance Entangling Gates in Three-Qubit Quantum Dot Spin Systems

Nooshin M. Estakhri

Ada Warren

Sophia E. Economou

Edwin Barnes

Follow this and additional works at: https://digitalcommons.chapman.edu/engineering_articles



Part of the [Other Electrical and Computer Engineering Commons](#), and the [Quantum Physics Commons](#)

Long-Distance Photon-Mediated and Short-Distance Entangling Gates in Three-Qubit Quantum Dot Spin Systems

Comments

This article was originally published in *Physical Review Research*, volume 6, in 2024. <https://doi.org/10.1103/PhysRevResearch.6.043029>

Creative Commons License



This work is licensed under a [Creative Commons Attribution 4.0 License](https://creativecommons.org/licenses/by/4.0/).

Copyright

Published by the American Physical Society.

Long-distance photon-mediated and short-distance entangling gates in three-qubit quantum dot spin systems


Nooshin M. Estakhri^{1,2,3,4,*}, Ada Warren^{3,4}, Sophia E. Economou^{3,4,†} and Edwin Barnes^{3,4,‡}

¹Fowler School of Engineering, *Chapman University*, Orange, California 92866, USA

²Institute for Quantum Studies, *Chapman University*, Orange, California 92866, USA

³Department of Physics, *Virginia Polytechnic Institute and State University*, Blacksburg, Virginia 24061, USA

⁴*Virginia Tech Center for Quantum Information Science and Engineering*, Blacksburg, Virginia 24061, USA

 (Received 24 October 2023; revised 14 December 2023; accepted 15 July 2024; published 11 October 2024)

Superconducting resonator couplers will likely become an essential component in modular semiconductor quantum dot (QD) spin qubit processors, as they help alleviate crosstalk and wiring issues as the number of qubits increases. Here, we focus on a three-qubit system composed of two modules: a two-electron triple QD resonator coupled to a single-electron double QD. Using a combination of analytical techniques and numerical results, we derive an effective Hamiltonian that describes the three-qubit logical subspace and show that it accurately captures the dynamics of the system. We examine the performance of short-range and long-range entangling gates, revealing the effect of a spectator qubit in reducing the gate fidelities in both cases. We further study the competition between nonadiabatic errors and spectator-associated errors in short-range operations and quantify their relative importance across practical parameter ranges for short and long gate times. We also analyze the impact of charge noise together with residual coupling to the spectator qubit on intermodule entangling gates and find that for current experimental settings, leakage errors are the main source of infidelities in these operations. Our results help pave the way toward identifying optimal modular QD architectures for quantum information processing on semiconductor chips.

DOI: [10.1103/PhysRevResearch.6.043029](https://doi.org/10.1103/PhysRevResearch.6.043029)

I. INTRODUCTION

Encoding qubits in the spin of electrons in electrostatically defined quantum dots (QDs), following the Loss-DiVincenzo proposal [1], continues to be one of the most promising platforms for future large-scale quantum processors [2,3]. Among the different types of QD-based quantum processors, silicon (Si)-based systems are especially promising due to their prospects for scalability and compatibility with existing semiconductor manufacturing processes [4–6]. Additionally, initialization, logical operations, and measurements can be conducted with all-electrical control signals [7,8]. Very high single-qubit gate fidelities (>99.9%) have been experimentally demonstrated for these qubits [9–14]. Also, two-qubit gates with fidelities higher than the 99% threshold for certain quantum error correcting codes [15] have been experimentally realized across different silicon-based QD platforms [9,13,14,16], with state preparation and measurement (SPAM) fidelities exceeding 97% [7,13]. Additionally, these processors can be designed to operate above one kelvin [17,18].

In these systems, single-qubit operations are commonly implemented by modulating the local electric confinement potential to oscillate the electron across a magnetic field gradient generated by micromagnets fabricated on top of the device. The resulting effective AC magnetic field rotates the spin in a process known as electric-dipole spin resonance (EDSR) [19–21]. On the other hand, two-qubit gates can be implemented by taking advantage of the Heisenberg exchange coupling between neighboring QDs [1,9,13,16,22–32]. This coupling can be turned on or off on nanosecond timescales by applying voltage pulses to either lower or raise the interdot barrier or by tilting the double well potential.

QD-based processors containing up to six fully operational spin qubits have been realized [33]. A promising approach to achieving processors with more qubits is to exploit modularity [34,35]. For example, architectures in which multiple few-qubit modules are connected by quantum interconnects such as superconducting resonators are particularly attractive for mitigating crosstalk and wiring issues. This, combined with techniques such as coherent spin shuttling [36,37], provides a route to reach larger QD processors.

Superconducting resonators are widely utilized for mediating long-range interactions between both superconducting qubits [38–40] and electronic spin qubits [41,42]. While magnetic dipole interactions between electron spins and resonator photons are only in the range of <kHz, strong spin-photon couplings in the range of tens of MHz may be reached by utilizing the electric dipole interaction in combination with spin-orbit couplings and EDSR techniques [43–48].

*Contact author: nmestakhri@chapman.edu

†Contact author: economou@vt.edu

‡Contact author: efbarnes@vt.edu

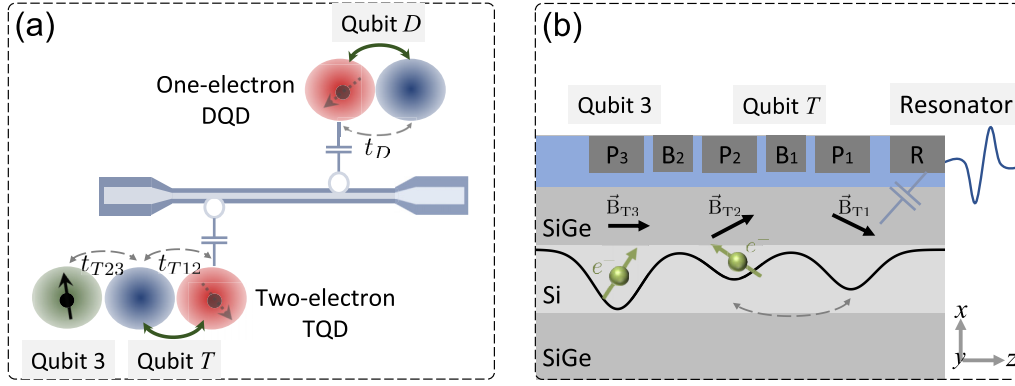


FIG. 1. (a) An abstract sketch of the three-qubit QD system composed of three main components: a two-electron TQD module, a single-electron DQD module, and a superconducting resonator as a quantum bus with virtual photons to mediate interactions. (b) Illustration of a two-electron TQD module capacitively coupled to a superconducting resonator based on gate-defined QDs in a Si/SiGe heterostructure. The plunger (P_1 , P_2 , and P_3) and barrier (B_1 and B_2) gates on top of the structure control the chemical potentials of the wells and the interdot tunnel couplings. Resonator electrode (R) capacitively couples dot 1 to a probe inside a superconducting resonator. A nearby micromagnet (not shown) creates a static magnetic field (\vec{B}) gradient between the first two dots with the arrangement of the magnetic field as illustrated. The depths of the potential wells are not shown to scale for illustrative purposes. The single-electron DQD module has a layout similar to the first two dots of the TQD module.

Importantly, by employing microwave photons as mediators, signatures of coherent remote spin-spin interactions have been observed in the resonant [41] and dispersive regime [42] in QD systems, together with the realization of iSWAP oscillations in the dispersive regime between the two distant semiconductor spin qubits [49], bringing us a step closer to multicore operations in these processors.

While all-electrical control enables fast gate operations, it has the unwanted side effect of exposing the qubits to incoherent charge noise, which is likely due to charge traps at interfaces in the semiconductor heterostructure [12,20,50–52]. These are dominant sources of decoherence in these systems and are important factors in designing processor architectures. Magnetic noise caused by hyperfine interactions with ^{29}Si nuclear spins can also be an issue. However, this can be largely mitigated by isotopic purification to reach low levels (50–800 ppm) [8,9,12,14,53] of residual ^{29}Si isotope concentrations, resulting in coherence times of up to a few milliseconds for spins in gate-defined QDs [12], and coherence times of up to 10 seconds for the spins of donor-bound electrons [53].

Despite these advances, theoretical studies of remote spin-spin coupling in semiconductor platforms have so far been limited to two qubits, in different coupling regimes, with one qubit in each module [54–59]. One needs to consider at least three qubits in order to investigate important issues such as the impact of spectator qubits on the performance of resonator-mediated gates. Another important question pertains to the quality of remote entangling operations between qubits that are not directly coupled to the resonator. It is also important to understand how charge noise spreads in modular, multiqubit systems and how its impact compares to other loss mechanisms, such as crosstalk and leakage.

In this paper, we analyze short-range and long-range entangling operations in a QD system with three spin qubits, in which one qubit is confined to a double quantum dot (DQD) that is resonator coupled to a triple quantum dot (TQD)

module containing two qubits. We examine the performance of short-range (intramodule) and long-range (intermodule) two-qubit entangling gates and explore the effect of spectator qubits. We also study the effect of charge noise on long-distance entangling gate fidelities in the presence of a spectator qubit, finding that the latter has a stronger impact on fidelities for typical experimental parameter regimes. Our work serves as a natural first step towards identifying optimal operating regimes for modular architectures containing multiple qubits connected by resonators.

The paper is organized as follows. In Sec. II, we introduce the structure of the resonator-mediated three-qubit system and outline the Hamiltonian, relevant parameters, and the notation. We then present an effective model that accurately captures the dynamics of the dressed spin system which is used to encode the qubits. In Sec. III, a protocol for implementing short-range entangling gates between two neighboring spin qubits is studied. Long-range entangling gates across the resonator and the effect of the quasistatic charge noise are presented in Sec. IV. Section V summarizes the results of the study.

II. THREE-QUBIT SYSTEM

A. Setup

We consider three electron spin qubits confined to gate-defined QDs. These QDs are created by applying DC voltages on gate electrodes located on the surface of a semiconductor heterostructure to isolate and confine three electrons from the two-dimensional (2D) electron gas that resides at an interface within the heterostructure. We consider a device containing a total of five QDs separated into two modules, one of which is a DQD containing one electron and the other a TQD with two electrons. The two modules are connected by a superconducting transmission line resonator, which capacitively couples to one QD from each module. Figure 1(a) shows a schematic representation of the hybrid Si-cQED device under study with

the three spin qubits in the system labeled. A more detailed illustration of the TQD module in this system is shown in Fig. 1(b). The DQD module, also connected to the resonator, has a configuration similar to the first two dots of the TQD module.

The electrical voltage signals applied to the plunger and barrier gate electrodes on top of the device control the electrostatic environments within the heterostructure and provide effective knobs to control the chemical potential level of all dots, ϵ_{Di} and ϵ_{Ti} , and the interdot tunnel couplings, t_D and t_{Tij} . Here, we label the two dots in the DQD by $D1$ and $D2$, while the three dots in the TQD are labeled $T1$, $T2$, and $T3$. The resonator couples to dots $D1$ and $T1$.

We assume that the device is functioning in a three-electron regime such that with proper voltage controls, the charge occupations are such that there is a single electron delocalized across the DQD (qubit D), a single electron delocalized across the first two dots of the TQD (qubit T), and one electron trapped in the third dot ($T3$) of the TQD module (qubit 3).

B. Hamiltonian

The Hamiltonian of the entire system can be represented by modeling the DQD module, TQD module, resonator, drive, and the interaction between the coupled parts, assuming $\hbar = 1$, as

$$\begin{aligned}
 \hat{H}_{\text{tot}} &= \hat{H}_r + \hat{H}_{\text{DQD}} + \hat{H}_{\text{TQD}} + \hat{H}_{\text{DQD-R}} + \hat{H}_{\text{TQD-R}} + \hat{H}_{\text{drive}}, \\
 \hat{H}_r &= \omega_r a^\dagger a, \\
 \hat{H}_{\text{DQD}} &= \sum_{i=1}^2 (\epsilon_{Di} n_{Di} + \vec{B}_{Di} \cdot \vec{S}_{Di}) \\
 &\quad - \sum_{\sigma=\uparrow,\downarrow} (t_D c_{D2\sigma}^\dagger c_{D1\sigma} + \text{H.c.}), \\
 \hat{H}_{\text{TQD}} &= \sum_{i=1}^3 \left[\epsilon_{Ti} n_{Ti} + \frac{U_{Ti}}{2} n_{Ti}(n_{Ti} - 1) + \vec{B}_{Ti} \cdot \vec{S}_{Ti} \right] \\
 &\quad + V_{T12} n_{T1} n_{T2} + V_{T23} n_{T2} n_{T3} + V_{T31} n_{T3} n_{T1} \\
 &\quad - \sum_{\sigma=\uparrow,\downarrow} (t_{T12} c_{T2\sigma}^\dagger c_{T1\sigma} + t_{T23} c_{T3\sigma}^\dagger c_{T2\sigma} \\
 &\quad + t_{T31} c_{T1\sigma}^\dagger c_{T3\sigma} + \text{H.c.}), \\
 \hat{H}_{\text{DQD-R}} &= 2g_D^{\text{AC}} (a^\dagger + a) n_{D1}, \\
 \hat{H}_{\text{TQD-R}} &= 2g_T^{\text{AC}} (a^\dagger + a) n_{T1}, \\
 \hat{H}_{\text{drive}} &= \Omega_D \cos(\omega_d t) (n_{D1} - n_{D2}), \tag{1}
 \end{aligned}$$

where \hat{H}_r describes the microwave resonator, while the \hat{H}_{DQD} and \hat{H}_{TQD} terms describe the DQD and TQD modules. The Hamiltonians for the DQD and TQD modules correspond to a single-band Fermi-Hubbard model. This Hamiltonian has been previously examined in the case of semiconductor quantum dot spin qubits [60,61]. The capacitive couplings between the resonator field mode and the charge occupation of the nearest dot to the resonator are modeled by the terms $\hat{H}_{\text{DQD-R}}$ and $\hat{H}_{\text{TQD-R}}$.

Here, $a^\dagger(a)$ is the bosonic creation (annihilation) operator of the resonator mode with the angular frequency ω_r

and $c_{i\sigma}^\dagger(c_{i\sigma})$ are the fermionic creation (annihilation) operators for an electron in dot i with spin σ . Operator n_k is the total number operator for dot k , i.e., $n_k = n_{k\uparrow} + n_{k\downarrow}$, with $n_{k\uparrow}$ ($n_{k\downarrow}$) being the number operator for the spin-up (-down) state in the dot k . The spin vector for dot k is $\vec{S}_k = \frac{1}{2}(c_{k\uparrow}^\dagger c_{k\downarrow} + c_{k\downarrow}^\dagger c_{k\uparrow}, \frac{c_{k\uparrow}^\dagger c_{k\downarrow} - c_{k\downarrow}^\dagger c_{k\uparrow}}{i}, c_{k\uparrow}^\dagger c_{k\uparrow} - c_{k\downarrow}^\dagger c_{k\downarrow})$. We assume that only one bosonic mode of the resonator is relevant to the dynamics of the system. Here we focus on entangling gate designs considering linear-array TQD structures, with only nearest-neighbor tunnel couplings, i.e., $t_{T13} = 0$, which is relevant to experimental developments. In such cases, any phases in the tunnel coupling parameters (t_D , t_{T12} , and t_{T23}) can be eliminated from the full-system Hamiltonian using unitary transformations. Specifically, without the loss of generality, the tunnel coupling t_D can be assumed real and positive using transformations $c_{D1\sigma} \rightarrow e^{-i \arg(t_D)} c_{D1\sigma}$ in the theoretical and numerical modelings; similarly, tunnel couplings t_{T12} , and t_{T23} can be considered positive and real with transformations $c_{T1\sigma} \rightarrow e^{-i \arg(t_{T12})} c_{T1\sigma}$ and $c_{T3\sigma} \rightarrow e^{i \arg(t_{T23})} c_{T3\sigma}$. In the plaquette geometries with nonzero t_{T13} , however, the remaining phase of t_{T13} cannot, in general, be eliminated and must be carefully considered as it may lead to nontrivial effects on the spin dynamics. Specifically, in the presence of magnetic fields, the Peierls phase needs to be included in numerical modelings of plaquette structures depending on the spatial profile of the fields and physical arrangements of the system. Inspired by recent experimental realizations and assuming the aforementioned transformations of the basis states, in our studies, the interdot tunnel couplings t_D , t_{T12} , and t_{T23} are considered to be real and positive, without the loss of generality. We also only include the ground states of the confinement potentials of the QDs in the orbital part of the Hilbert space since the excited orbital states are at sufficiently higher energies. The chemical potentials of the dots are denoted by ϵ_{Di} and ϵ_{Ti} , and the interdot tunnel couplings are captured by the t_D and t_{Tij} parameters, determined by the spatial overlap of the wave functions in the dots. In practice, both sets of parameters can be electrically tuned using gate electrodes. U and V are the intra- and interdot Coulomb repulsion energies, respectively, and they are found to be typically in the range of a few to ten meV [60,61]. To impose the condition that one electron in the TQD module gets localized to dot $T3$ with high probability, we impose $\epsilon_{T3} \ll \epsilon_{T2} + V_{T12} - V_{T31}$, $\epsilon_{T1} + V_{T12} - V_{T23} \ll U_{T1}$, U_{T2} , U_{T3} in all the analyses that follow.

While the effect of intrinsic spin-orbit interactions can be ignored, artificial spin-orbit interactions are engineered by placing micromagnets on top of the device and creating magnetic field gradients across neighboring dots. Leveraging this technique, the interaction between the spin of delocalized electrons and the electric field from the resonator is mediated through electric dipole interactions [43], leading to higher effective spin-photon coupling strengths [45–48] and therefore practical two-qubit interaction times. The electric dipole coupling strengths for coupling to the resonator fields are denoted by g_D^{AC} and g_T^{AC} for the DQD and TQD modules, respectively. The total magnetic field vector, including the external field as well as that generated by the micromagnets, in dot i of DQD and TQD, is denoted by \vec{B}_{Di} and \vec{B}_{Ti} . In the numerical studies that follow, the average magnetic field in the DQD and the

first two dots of the TQD are chosen along the z direction, while the magnetic field gradient is along the x axis to induce transverse spin-orbit couplings. The magnetic field in the third dot of the TQD is along the z direction [Fig. 1(b)].

The Hamiltonian of Eq. (1) also includes an electric drive term on the potentials of the dots in the DQD module with amplitude $\tilde{\Omega}$ and frequency ω_d . This drive is used in the implementation of a long-range maximally entangling gate (in this case, CNOT), as discussed in Sec. IV.

For the one- and two-electron charge configurations assumed above for the DQD and TQD modules, respectively, the single-particle subspace of the DQD has a dimensionality of four, with computational basis states given by $c_{D1\uparrow}^\dagger|0\rangle$, $c_{D1\downarrow}^\dagger|0\rangle$, $c_{D2\uparrow}^\dagger|0\rangle$, $c_{D2\downarrow}^\dagger|0\rangle$, while the two-particle subspace of the TQD has a dimensionality of 15, with computational basis states given by $c_{T1\uparrow}^\dagger c_{T3\uparrow}^\dagger|0\rangle$, $c_{T1\uparrow}^\dagger c_{T3\downarrow}^\dagger|0\rangle$, $c_{T1\downarrow}^\dagger c_{T3\uparrow}^\dagger|0\rangle$, $c_{T1\downarrow}^\dagger c_{T3\downarrow}^\dagger|0\rangle$, $c_{T2\uparrow}^\dagger c_{T3\uparrow}^\dagger|0\rangle$, $c_{T2\uparrow}^\dagger c_{T3\downarrow}^\dagger|0\rangle$, $c_{T2\downarrow}^\dagger c_{T3\uparrow}^\dagger|0\rangle$, $c_{T2\downarrow}^\dagger c_{T3\downarrow}^\dagger|0\rangle$, $c_{T1\uparrow}^\dagger c_{T2\uparrow}^\dagger|0\rangle$, $c_{T1\uparrow}^\dagger c_{T2\downarrow}^\dagger|0\rangle$, $c_{T1\downarrow}^\dagger c_{T2\uparrow}^\dagger|0\rangle$, $c_{T1\downarrow}^\dagger c_{T2\downarrow}^\dagger|0\rangle$, $c_{T2\uparrow}^\dagger c_{T2\downarrow}^\dagger|0\rangle$, $c_{T3\uparrow}^\dagger c_{T3\downarrow}^\dagger|0\rangle$. It should be noted that although the multiqubit dynamics are purposely designed to primarily happen in the low-energy subspace of the full system Hamiltonian, all the simulations are carried out over the entire Hilbert space of Eq. (1), after we truncate the maximum resonator photon number to $n_r - 1$ i.e., a total of n_r photonic states. This results in a total system Hilbert space dimension of $60n_r$ that we use in our numerical simulations below.

In this work, we focus on TQDs arranged in a linear array, i.e., the three QDs sit on a line [see Fig. 1(a)], with only nearest-neighbor tunnel couplings, i.e., $t_{13} = 0$. This scheme is relevant to physical implementations of gate-defined QD-based quantum processors that have been the subject of investigations recently [33].

C. Testing the effective model

We consider the case of a dispersive regime, where coupling terms are sufficiently small relative to energy differences, and the drives are weak and detuned and can be considered perturbatively in the analysis. By applying frame transformations and a time-dependent Schrieffer-Wolff transformation [62], the coupling between the low-energy subspace and the rest of the Hilbert space is removed to the leading order (see Appendix A for the details of the derivation). Next, we project onto the low-energy subspace defined as the empty-cavity limit, i.e., $\langle a^\dagger a \rangle = 0$, and the ground state for the orbital degree of freedom of the DQDs, i.e., $\forall i \in \{D, T\} : \langle \tau_i^z \rangle = -1$, through which we derive an effective Hamiltonian, without the drive, governing the dynamics of the low-energy qubits,

$$\hat{H}_{\text{eff}} = \sum_{i=D,T,3} \frac{1}{2} \omega_i \sigma_i^z - J_r \sigma_D^x \sigma_T^x + \frac{J_e}{4} \vec{\sigma}_T \cdot \vec{\sigma}_3 + J_{ZZ} \sigma_T^z \sigma_3^z. \quad (2)$$

Here the effective Hamiltonian is composed of six terms. The first three terms represent the three dressed qubits with transition frequencies ω_i , $i \in \{D, T, 3\}$. The fourth term describes the long-distance resonator-mediated coupling between qubits

D and T with strength J_r . The fifth term corresponds to a short-distance exchange coupling between qubits T and 3 with strength J_e . The last term is a residual short-distance Ising coupling with strength J_{ZZ} between qubits T and 3 resulting from spin-charge hybridization. For the parameter regimes considered in this paper, this residual coupling is small and can be safely ignored if desired. A key observation here is that the structure of the effective Hamiltonian is comprised of two bipartite interactions, each between two neighboring qubits, as one might anticipate. However, the coupling strengths of these interactions depend on the details of the entire system (see Appendix A for the definitions of the effective parameters).

By engineering the dynamics in an unpopulated resonator mode, long-distance interactions are mediated via the exchange of virtual photons. The benefits of choosing such a subspace are twofold. First, the cavity-induced losses are effectively removed; and second, operations through the quantum bus between different sets or groups of modules can be parallelized, as interactions are merely virtual and no real populations are induced in the resonator, thus increasing the information processing speed and the throughput of the system.

Next, we put the derived effective Hamiltonian to the test through a numerical fitting approach, as described below. Confirming the validity of the effective Hamiltonian is important since we will use it extensively later on to devise protocols for implementing entangling operations between pairs of qubits.

We start by finding the time evolution of the whole system, $U_{\text{tot}}(t) = e^{-it\hat{H}_{\text{tot}}}$ for $t \in [0, t_0]$, followed by projection onto the low-energy subspace with the projection operator P , which yields the actual time evolution of the low-energy subspace $U_{\text{actual}}(t) = P U_{\text{tot}}(t) P$. The details of the projection operation and low-energy subspace are introduced in Appendix A. We then compare the actual time evolution with its counterpart based on the effective model, $U_{\text{eff}}(T) = e^{-iT H_{\text{eff}}}$. The metric for this comparison is the transformation fidelity defined as $F = \frac{dF_e + 1}{d + 1}$, where $F_e = \frac{1}{d^2} |\text{Tr}[U_{\text{actual}}^\dagger(t) U_{\text{eff}}(t)]|^2$ is the process fidelity [63] and d is the subspace dimension. We optimize this fidelity with respect to all the parameters of the effective model to find the best effective parameters (Fig. 2). Optimizing for only one point in the evolution time results in an infinite number of optimal parameter values, all giving the same fidelity, due to a periodic dependence on the parameters. To resolve this issue, we instead optimize the average fidelity over a sample of points during a time interval. The starting values in these optimizations are the analytically derived effective parameters (see Appendix A) and numerical simulations are truncated at three resonator levels. A time duration of $t_0 = 20 \mu\text{s}$ is used for the optimization procedure.

Figure 2 shows the transition frequencies of the dressed qubits and the resonator-mediated and exchange interaction strengths as a function of the detuning (i.e., the tilt of a double well potential), ϵ , of the DQD and the first two dots of the TQD module. The dots in the figure correspond to numerically found quantities from the fitting scheme explained above, and the lines correspond to the same parameters obtained from the effective model. The parameters used in the simulation are reported in the figure caption. The fidelity of the fit is

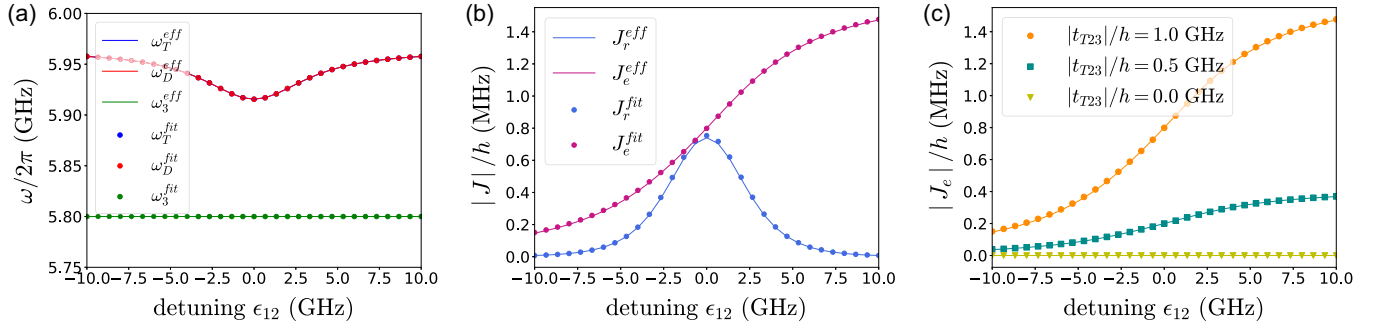


FIG. 2. Numerically derived values of the effective Hamiltonian parameters (dots) and the same parameters calculated from the analytically derived effective model (lines) for the (a) dressed qubits' transition frequencies, (b) resonator-mediated coupling strength, and (b),(c) exchange-enabled coupling strengths vs the detuning, ϵ , of the DQD and the first two dots of the TQD module. Parameters are set at $\omega_r/2\pi = 6$ GHz, $\omega_T^z/2\pi = \omega_D^z/2\pi = 5.95$ GHz (z -directed magnetic field strength in the DQD and the first two dots of the TQD), $\omega_3^z/2\pi = 5.8$ GHz (z -directed magnetic field strength in the third dot of TQD, with no x component), $t_D/h = t_{T12}/h = 3.5$ GHz, $t_{T23}/h = 1$ GHz (a),(b), $t_{T23}/h = 0, 0.5, 1$ GHz (c), $g_T^x/2\pi = g_D^x/2\pi = 200$ MHz, $g_D^{AC}/2\pi = g_T^{AC}/2\pi = 40$ MHz, $\epsilon_{T3}/h = -300$ GHz, $U_{T1}/h = U_{T2}/h = U_{T3}/h = 2.5$ THz.

greater than 97.5%, with a small residual coupling strength of $|J_{ZZ}|/h < 4$ kHz.

The fact that for all quantities the numerically found effective values are nearly identical to the matching values from the analytical model confirms that the effective model accurately captures the behavior of the low-energy three-qubit computational space and can be safely used to understand the dynamics of the system and devise gate protocols. Next, we study gate designs for short-range and long-range entangling gates, in the regime where the effect of the spectator qubit is suppressed, and we examine the interference caused by the spectator qubit on the fidelity of two-qubit operations. The simulation parameters employed throughout this work are chosen to be consistent with values from recent experimental works [9,13,37,47].

III. SHORT-RANGE ENTANGLING GATES

In this section, we describe and compare several protocols for implementing short-range entangling gates between qubits T and 3 within the TQD module. We focus on the implementation of CPHASE gates, which, in combination with single-qubit gates, yields a universal quantum gate set.

The effective two-qubit interaction between the qubits in the TQD module [Eq. (2)], in the regime where the effect of the third qubit is suppressed, is essentially in the form of an extended Heisenberg interaction between the two dressed spins residing in the TQD module,

$$\hat{H}_{\text{eff}, J_r \rightarrow 0} = \frac{1}{2}\omega_D\sigma_D^z + \frac{1}{2}\omega_T\sigma_T^z + \frac{1}{2}\omega_3\sigma_3^z + \frac{J_e}{4}\vec{\sigma}_T \cdot \vec{\sigma}_3. \quad (3)$$

In view of this, in principle, different techniques may be employed to realize two-qubit operations, such as AC-pulsed frequency-selective CROT and CNOT gates [16,22–24], DC-pulsed [25–27] and resonantly driven SWAP [28,29] gates, and CPHASE gates [9,13,24,30–32].

A. CPHASE gate operation region

Two-qubit gate implementations primarily depend on the strength of the exchange coupling, J_e , relative to the difference in the energy splittings of the two qubits, $\Delta\omega = |\omega_T - \omega_3|$.

For $J_e \gg \Delta\omega$, the exchange interactions result in SWAP evolutions, as the eigenstates of the two-qubit space are the spin singlet and triplets, which was, in fact, the original proposal to achieve entangling gates in QDs [1]. This regime is accessible by making the DQD energy levels highly detuned (to approximately 10–15 GHz range [25]), reaching a few GHz strength [25–27] for the interdot exchange couplings, making SWAP operations accessible.

Considering that charge noise is one of the important sources of incoherent noise in these electrically controlled systems [12,20,52,56,64], it is crucial to make gate protocols that can be applied in the regimes where the impact of this noise source is small. In multielectron regimes, exploiting dot anharmonicity has been shown to produce optimal working points to suppress the charge-noise-induced dephasing in five-electron DQD hybrid qubits [52]. Comparably, when a DQD with single electron is tuned to the symmetric operation point (zero detuning), the effect of the charge noise is suppressed to first order [65–67], resulting in longer coherence times. However, only smaller values of J_e are typically accessible at these points, and to get larger J_e the operation point needs to be moved away from the symmetric point, causing more decoherence in the system [25]. Besides, many QD spin qubit systems utilize large magnetic field gradients, enabling the addressability of the qubits. In practice, exchange coupling strengths are in the range of hundreds of kHz to 10–20 MHz [9,37], which is much smaller than the difference in the transition frequencies of the neighboring qubits, which is typically hundreds of MHz to GHz [9,37].

For these reasons, here we focus on the $J_e \ll \Delta\omega$ regime, which is naturally relevant for gate-defined QDs with micromagnet-induced magnetic field gradients and tunnel barrier-controlled exchange couplings. Evolution under an exchange interaction in this regime leads to a CPHASE gate between the two qubits [68,69]. CROT gates can also be achieved in this regime by selectively driving one of the EDSR transitions, in order to make a universal gate set. We investigate fast adiabatic CZ gates between qubits T and 3 , which may be implemented by applying a pulse to the barrier gate between dots 2 and 3 of the TQD module to temporarily modify the exchange coupling, while qubit D evolves in isolation.

B. Fast CZ gate and minimizing nonadiabatic errors

The exchange-based CZ gate can be realized due to the fact that a nonzero exchange interaction J_e , in the regime of $J_e \ll \Delta\omega$, lowers the energy of states with antiparallel spins, $|\uparrow\downarrow\rangle, |\downarrow\uparrow\rangle$, i.e., the odd-parity subspace, compared to the case with $J_e = 0$. This energy shift of antiparallel spins makes it possible to add spin-dependent phase shifts to the odd-parity subspace and thus realize CZ gates in the equivalent evolution form of $\text{diag}[1, \exp(i\phi_{\uparrow\downarrow}), \exp(i\phi_{\downarrow\uparrow}), 1]$ [68,69]. Here, $\phi_{\uparrow\downarrow}(\phi_{\downarrow\uparrow}) = \delta E_{\uparrow\downarrow}(\downarrow\uparrow)t_{\text{wait}}$, where t_{wait} is the evolution time, while $\delta E_{\uparrow\downarrow}(\downarrow\uparrow)$ is the energy shift of the dressed antiparallel eigenstates $|\uparrow\downarrow\rangle$ and $|\downarrow\uparrow\rangle$ relative to the states $|\uparrow\uparrow\rangle$ and $|\downarrow\downarrow\rangle$ as a consequence of the exchange interaction. A CZ gate is realized for $\phi_{\uparrow\downarrow} + \phi_{\downarrow\uparrow} = (2n+1)\pi$ up to local Z gates on qubits one and two. These local Z rotations can be implemented virtually by changing the phases of subsequent pulses and rotating the frame [70]. For $J_e \ll \Delta\omega$, the energy shift of the dressed eigenstates, to first order in J_e , is equal to $J_e/2$, creating CZ gates at gate time $t_g = (2n+1)\pi/\bar{J}_e$, where the time-averaged exchange coupling is defined as $\bar{J}_e = \frac{1}{t_g} \int_0^{t_g} J_e(t) dt$. Additionally, a spin-echo mechanism, adding midsequence π rotations on both spins about the x axis, can be incorporated to eliminate excess phases during the CZ exchange gate due to noisy unbalanced magnetic fields or local quasistatic phase noise, making the evolution in the even-parity subspace effectively trivial [69].

Although rectangular pulses can be used to generate CZ gates, the intrinsic nonadiabatic nature of such pulses results in coherent errors in the gate dynamics, causing reduced gate fidelities. Since turning on and off the exchange interaction only affects the odd-parity subspace of the effective two-QD system, the full dynamics of the system can be designed by simply engineering the dynamics of the odd-parity subspace spanned by the $|\uparrow\downarrow\rangle, |\downarrow\uparrow\rangle$ states, with effective Pauli operators defined as $\sigma'_x = |\uparrow\downarrow\rangle\langle\downarrow\uparrow| + |\downarrow\uparrow\rangle\langle\uparrow\downarrow|$ and $\sigma'_z = |\uparrow\downarrow\rangle\langle\uparrow\downarrow| - |\downarrow\uparrow\rangle\langle\downarrow\uparrow|$, in terms of which the Hamiltonian in this subspace is

$$\hat{H}_{\text{odd}} = \frac{1}{2}[-J_e(t) + \Delta\omega\sigma'_z + J_e(t)\sigma'_x]. \quad (4)$$

The requirement for the CZ operation is now a global phase shift in this subspace, while SWAP-like operations due to the nonadiabatic nature of the pulse translate to nontrivial dynamics in the subspace and therefore must be suppressed. The evolution in the odd-parity subspace can be visualized in terms of a Bloch sphere trajectory controlled by the Hamiltonian vector $(J_e/2, 0, \Delta\omega/2)$. In this case, Ref. [71] showed that the nonadiabatic error P_e is proportional to the power spectral density of the rate of change of the control Hamiltonian, $d\theta/dt$, with θ being the angle of the Hamiltonian vector with respect to the quantization axis z , calculated at the precession frequency ω_q as $P_e = (1/4)S_{d\theta/dt}(\omega_q)$, in which S denotes the power spectral density. The precession frequency is the difference in the eigenenergies of the two-dimensional subspace, which, based on Eq. (4), is given by $\omega_q = \sqrt{J_e^2 + \Delta\omega^2}$.

Now, with the assumption of $J_e \ll \Delta\omega$, which is relevant to the case studied here, the nonadiabatic error will be relatively small, and the connection between the nonadiabatic error and the power spectral density of the signal holds in this

small-error limit. This is due to the large precession frequencies of the Bloch vector (around the Hamiltonian vector) compared to the relatively slower time dependence of the change in θ over the Bloch sphere. For the Hamiltonian (4), the direction of the ground eigenstate Bloch vector is antiparallel with the Hamiltonian vector, and therefore the rate of change of the control field is proportional to the rate of change of the instantaneous eigenstates of the system. To have simply a global phase in the odd-parity subspace, the Hamiltonian vector should not deviate much from the z axis, consistent with the condition of $J_e(t) \ll \Delta\omega$. We specifically study two cases: (i) a rectangular pulse with constant J_e during the gate time, corresponding to a fixed θ during the pulse, and (ii) smooth J_e signals using window functions, for which θ slowly varies from zero to a maximum angle and then returns. Both control schemes have been experimentally utilized to generate CZ gates. See Refs. [13,24,31,32] for CZ gates with rectangular control signals and Refs. [9,30] for CZ gates with Hann signals.

The rate of nonadiabatic errors can be investigated by moving to the adiabatic frame of the system, using the transformation $T = \exp\{-i \arctan[J_e(t)/\Delta\omega]\sigma'_y/2\}$ or, equivalently, by analyzing the change in the Hamiltonian angle $d\theta/dt \approx \dot{J}_e/\Delta\omega$, resulting in nonadiabatic errors, $P_e \propto S_{(J_e/\Delta\omega)}(\omega_q)$.

With the rectangular CZ pulse, $J_e(t) = J_0/2$, $0 < t < t_g$, the CZ gate is reached at $t_g = 2\pi/J_0$, and the nonadiabatic error is given by $P_e^{\text{rect}} \propto \frac{1}{\alpha} \sin^2(\omega_q t_g/2)$ with $\alpha = (\Delta\omega t_g/\pi)^2$. The smallest gate time at which the nonadiabatic error is minimized is $t_g = 2\pi/\omega_q$ (synchronization). However, these pulses have an infinitely fast rise and fall, which is not quite practical due to the cutoff frequencies of the control electronics. Also, the fall-off rate of the nonadiabatic error with increasing gate time is quite slow ($\sim 1/t_g^2$) for these pulses. Besides, it is crucial to have stable control signals, such that the error does not increase rapidly under small changes in the applied signal. Because of these factors, smooth control pulses that perform in a way that is insensitive to slight variations in the waveform shape are generally of interest.

These issues can be addressed by replacing the rectangular pulse with a smooth pulse that optimizes the energy spectral density. This is a known task in the field of signal processing [72], and here we leverage some prior results from that literature to study gates for our three-qubit system. We employ the Hann window function, $W_{\text{Hann}}(t) = \frac{1}{2}[1 - \cos(2\pi t/t_g)]$, which is an extensively used function in signal processing and is essentially the first-order Fourier window function. For the Hann pulse, $J_e(t) = J_0 W_{\text{Hann}}$, the CZ gate is again reached at $t_g = 2\pi/J_0$. The nonadiabatic error can be calculated as $P_e^{\text{Hann}} \propto \frac{1}{\alpha} \sin^2(\omega_q t_g/2)/|1 - (\omega_q t_g/2\pi)^2|^2$ with the same α parameter as P_e^{rect} .

After choosing this temporal profile for the exchange coupling, in the next step, we use numerical interpolation techniques to arrive at the required interdot tunnel coupling $t_{T23}(t)$, based on the effective Hamiltonian values. A sample $t_{T23}(t)$ with a Hann window function is shown in Fig. 3(b). For all gate analyses in this work, we numerically solve the Schrödinger equation with the Hamiltonian in Eq. (1). We then project the time evolution at each time step onto the

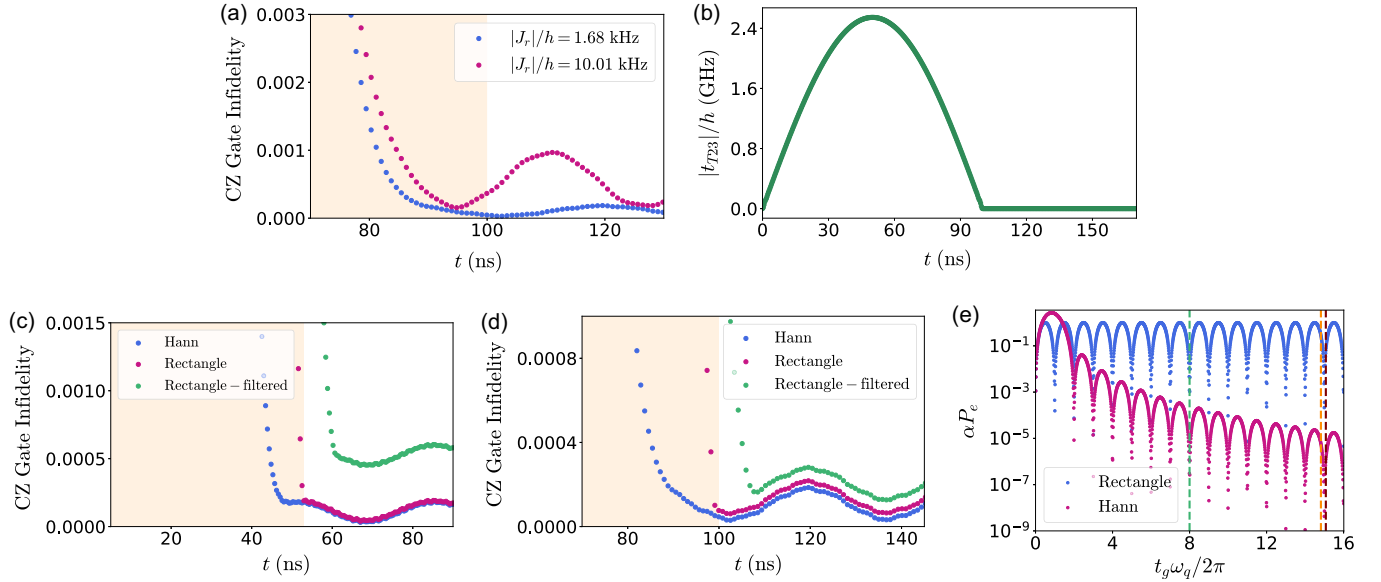


FIG. 3. Short-range CZ gate in the TQD module through fast adiabatic evolution. (a) CZ gate infidelity vs time for a gate time of $t_g = 100$ ns (light-orange shading). Results for two values of the effective resonator-mediated coupling J_r/h to the spectator qubit (qubit D) are shown. (b) Temporal profile of the tunnel coupling when a Hann window function is used for the CZ gate in (a) with $|J_r|/h = 1.68$ kHz. (c) CZ gate infidelity for synchronized evolutions with $t_g \omega_q / 2\pi = 8$ for Hann, rectangular, and filtered rectangular pulses. (d) CZ gate infidelity for evolutions with $t_g = 100$ ns for Hann, rectangular, and filtered rectangular pulses. (e) Normalized nonadiabatic error spectral profile for rectangular and Hann window functions. The red and orange dashed vertical lines indicate the parameter regime for the results in (a) for $|J_r|/h = 1.68$ and 10.01 kHz, respectively. The green dashed line shows the parameter regime of (c). All gate fidelities are optimized over local operations on all qubits at each time step. Additional system parameters for (a)–(d) are $\omega_r/2\pi = 6$ GHz, $\omega_T^z/2\pi = 5.94$ GHz, $\omega_D^z/2\pi = 5.96$ GHz, $\omega_3^z/2\pi = 5.8$ GHz, $|t_D|/h = |t_{T12}|/h = 3.5$ GHz, $t_{T23} = t_{T23}(t)$, $g_T^x/2\pi = g_D^x/2\pi = 200$ MHz, $g_D^{AC}/2\pi = g_T^{AC}/2\pi = 50$ MHz, $\epsilon_{T3}/h = -300$ GHz, and $U_{T1}/h = U_{T2}/h = U_{T3}/h = 2.5$ THz. $|J_r|/h = 1.68$ kHz in (b)–(d).

low-energy subspace, effectively tracing out the resonator and higher-energy orbital degrees of freedom to arrive at the evolution of the three-qubit computational subspace.

We quantify the performance of multiqubit gates using the average gate fidelity $F = \frac{1}{d(d+1)} (\text{Tr}[UU^\dagger] + |\text{Tr}[U^\dagger U_{\text{goal}}]|^2)$ [63], in which d is the dimension of the Hilbert space on which the gate acts, U is the actual evolution operator of the system, and U_{goal} is the target evolution. In principle, entangling operations between two qubits in multiqubit processors should not affect the rest of the qubits in the system, i.e., the evolution operator for the rest of the qubits should be either trivial or merely in the form of local operations which can be compensated after the two-qubit operation. To capture this crucial concept in our three-qubit system, in all gate analyses throughout this work, the reported two-qubit (CZ or CNOT) gate fidelities refer to three-qubit gate fidelities relative to a block-diagonal target gate that includes the ideal two-qubit gate in one block and a single-qubit operation on the other, i.e., $U_{\text{goal}}^{\text{CZ}} = \text{CZ}_{T3} \otimes I_D$ for this section and $U_{\text{goal}}^{\text{CNOT}} = \text{CNOT}_{TD} \otimes I_3$ for Sec. IV. In trying to realize this target operation, we minimize the degree to which the two-qubit gate affects the quantum information encoded in the third qubit.

Figure 3(a) shows the infidelity ($1 - F$) of fast adiabatic CZ gates between qubits T and 3 and local operations on qubit D as a function of time for a pulsed exchange coupling J_e with a Hann window function profile and 100 ns gate time. Results for two different values of the coupling to the spectator qubit,

which is qubit D in this case, are shown. In particular, we consider $|J_r|/h = 1.68$ and 10.01 kHz, which are calculated from the effective Hamiltonian model for two detuning values, $\epsilon_T/h = \epsilon_D/h = 15$ and 10.5 GHz, respectively. The gate fidelities shown in the figure are optimized over local operations. The temporal profile of the $|t_{T23}(t)|$ tunnel coupling for $|J_r|/h = 1.68$ kHz is shown in Fig. 3(b) for $J_0/h = 10$ MHz. The temporal extents of the applied control signals, $t_{T23}(t)$, are marked with a light-orange background on all infidelity plots.

Here the infidelities are found to be better than 1.86×10^{-4} and 9.68×10^{-4} in the two cases, respectively, from which it can be concluded that by adjusting the detunings of the DQDs to within the range quoted above, the effect of the spectator qubit on the short-distance CZ gate is negligible. The CZ gate infidelities exhibit oscillatory behavior after the pulse time t_g , and the infidelities given above correspond to the highest infidelities observed for all cases reported in this section. The unitarity of the evolution in the logical subspace is also better than 0.9998 and 0.9989, respectively. Similar CZ gate implementations with the Hann window function have been recently employed experimentally in two-qubit processors [9,30], with very high fidelities (99.65% for [9]) observed.

Higher-order Fourier-basis window functions, $J_e(t) = J_0 \sum_n \lambda_n [1 - \cos(2\pi n t/t_g)]$ may also be used for spectral engineering, where the Hann window function corresponds to the special case of a first-order window. The higher-order

functions can also be optimized to minimize the nonadiabatic error for any time larger than a chosen time and have power densities that decrease with increasing order. Since these Fourier-basis windows are natural extensions of the Hann window and can potentially further reduce the error, we also analyzed second- and fourth-order Fourier-basis windows with optimized Fourier coefficients λ_n [71] for the implementation of CZ gates for the same system parameters as in Fig. 3(a). We find an almost negligible (less than 5×10^{-7}) change in the infidelities for both higher-order windows compared to the Hann window, indicating that there is little benefit to using the higher-order functions. This is due to the fact that here $t_g \omega_q / 2\pi \approx 15.08$, and so nonadiabatic error rates are essentially overshadowed by the infidelities due to the presence of the spectator qubit as well as the coupling to the nonempty resonator states and higher orbitals.

C. Synchronization and finite bandwidths of control electronics

Though it may seem to be favorable to work in the regime with higher $t_g \omega_q / 2\pi$ [see Fig. 3(e)] to reduce coherent errors due to SWAP-like evolutions, for the fixed difference in transition frequencies determined from the experiment, this condition translates to longer gate times and consequently greater decoherence. On the other hand, reducing the gate time requires larger exchange couplings, which may not be feasible in some experiments. The connection between the nonadiabatic errors and the spectral profile of the pulse enables one to design pulses that match the zeros of the power spectral density function to significantly reduce the nonadiabatic error via synchronization. We next examine this approach in the presence of the spectator qubit, while also considering the finite bandwidth of the control electronics.

The error spectra of the Hann and rectangular window functions have zeros at $t_g = 2\pi m / \omega_q$ ($m \in \mathbb{Z}_+$ for rectangular and $m \in \mathbb{Z}_+ \setminus \{1\}$ for Hann windows), which may be synchronized with the CZ gate time to reach a phase of $(2n + 1)\pi$ in the odd-parity subspace. This results in a gate time of

$$t_g^{\text{sync}} = \frac{\pi}{\Delta\omega} \sqrt{4m^2 - (2n + 1)^2}. \quad (5)$$

Figure 3(c) shows the CZ gate infidelities for $t_g \omega_q / 2\pi = 8$, which is matched with a gate time of $t_g = 52.98$ ns for the Hann and rectangular window functions, as well as for a low-pass-filtered rectangular function, for a spectator qubit coupling of $|J_r|/h = 1.68$ kHz. A Butterworth filter of order six is used here, with a cutoff frequency of 100 MHz to filter the $t_{T23}(t)$ function. The green dashed line in Fig. 3(e) indicates the region associated with these pulses, with the maximum value of the exchange coupling being less than 20 MHz, consistent with the recently reported [9] range of 100 kHz to 20 MHz. For the Hann, rectangular, and filtered rectangular pulses, the oscillatory infidelity functions after the pulse reach maximum infidelities of 1.84×10^{-4} , 1.92×10^{-4} , and 6.04×10^{-4} , respectively. A key observation is that for the rectangular pulses, fidelities as good as those achieved for longer CZ gates [Fig. 3(a)] may be reached, yet for much shorter pulses of time, $t_g = 52.98$ ns. However, by limiting the bandwidth of the pulse, the gate infidelity increases by

approximately a factor of three, as we can see by comparing results for the filtered and unfiltered rectangular functions.

Next, to distinguish between the effect of nonadiabatic error and bandwidth limitations on the control signals, we examine the CZ evolution for a longer gate time of $t_g = 100$ ns for different pulse shapes. The results are shown in Fig. 3(d), where infidelities as low as 1.86×10^{-4} , 2.18×10^{-4} , and 2.82×10^{-4} are achieved for Hann, rectangular, and filtered rectangular pulses, respectively. Comparing Hann and rectangular pulses and with the results of Figs. 3(a) and 3(c), it can be concluded that the nonadiabatic errors are no longer the limiting factor in the range of $t_g \gtrsim 100$ ns pulses. Also, we find that low-pass filtering of the pulse adds an additional infidelity penalty of 6.4×10^{-5} . Additionally, we conclude that with this amount of coupling to the spectator qubit, operations with Hann or perfect rectangular pulses, for both synchronized short and long gate times, lead to roughly similar levels of infidelity. On the other hand, for short pulses without the synchronization condition satisfied, rectangular pulses lead to much higher infidelities compared to Hann pulses, as can also be concluded from Fig. 3(e). For example, for an asynchronous evolution of $t_g \omega_q / 2\pi = 8.5$ corresponding to a gate time of $t_g = 56.3$ ns, the rectangular pulse only reaches 1.74×10^{-3} infidelity, while the Hann pulse still gives the same 1.83×10^{-4} level of infidelity. Therefore, the importance of using window functions for shorter gate times, even if high bandwidth pulses are available, is undeniable. To explore this point in more detail, we have also studied fast adiabatic CZ gates between qubits T and 3 with piecewise constant exchange pulses—see Appendix B. Despite all the advantages in mitigating nonadiabatic errors, Hann window functions have a big disadvantage. They require twice the interdot coupling strength at the maximum point compared to the rectangular pulses. Therefore, limitations on available coupling strengths may make it hard to experimentally test these shorter pulses.

IV. LONG-RANGE ENTANGLING GATES

A resonator-mediated CNOT gate can be implemented by applying a microwave drive to modulate the energy levels of the DQD module to create a significant interaction with qubit T in the TQD. In this scheme, qubit D is the control and qubit T is the target of the CNOT gate, with qubit 3 being the spectator. This protocol has been previously employed theoretically [57] in QD systems with two spins. In this section, we review this technique and apply it in the case of a three-qubit system, enabling us to also study the effect of the spectator qubit.

A. Cross-resonance CNOT gate

In the absence of the spectator qubit, the microwave drive added to the DQD module results in the effective two-qubit low-energy Hamiltonian $\hat{H}_{\text{eff}} = \frac{1}{2} \omega_D \sigma_D^z + \cos(\omega_d t) (\Omega_{\text{eff}}^z \sigma_D^z + \Omega_{\text{eff}}^x \sigma_D^x) + \cos(2\omega_d t) (\xi_D^z \sigma_D^z + \xi_D^x \sigma_D^x) + \sin(2\omega_d t) \xi_D^y \sigma_D^y + \frac{1}{2} \omega_T \sigma_T^z - J_r \sigma_D^x \sigma_T^x$ in the laboratory frame, with $\Omega_{\text{eff}}^x = \sin(\beta_D) \Omega_D$, $\Omega_{\text{eff}}^z = \xi_D^z = \xi_D^y = \xi_D^x = 0$, $J_r = \omega_r g_D^{\text{AC}} g_T^{\text{AC}} \sin(\beta_D) \sin(\beta_T) \times \{1/[\omega_r^2 - (\omega_D^{\text{AC}})^2] + 1/[\omega_r^2 - (\omega_T^{\text{AC}})^2]\}$ for zero detunings, $\epsilon_T = \epsilon_D = 0$ [57]. Next, by applying a frame transformation, $U_1 = \exp[-it\omega_d(\sigma_D^z +$

$\sigma_T^z)/2]$, the Hamiltonian can be moved to the doubly rotating frame, and the rotating wave approximation can be made to remove the rapidly oscillating terms from the Hamiltonian, followed by another transformation using $U_2 = \exp[-i\chi\sigma_D^y/2]$, in which $\chi = \arctan(\Omega_{\text{eff}}^x/\delta_D)$ and $\delta_D = \omega_D - \omega_d$, to arrive at the Hamiltonian in the diagonalized doubly rotating frame. Next, we transfer to the quadruply rotating frame using another time-dependent frame transformation, $U_3 = \exp[-it(\eta\sigma_D^z + \delta_T\sigma_T^z)/2]$ with $\eta = \sqrt{\delta_D^2 + (\Omega_{\text{eff}}^x)^2}$ and $\delta_T = \omega_T - \omega_d$ [57]. The final form of the Hamiltonian in this quadruply rotating frame is

$$H_{\text{QF}} = -J_r(\cos(\omega_d t)\{\sin(\chi)\sigma_D^z + \cos(\chi)[\cos(\eta t)\sigma_D^x - \sin(\eta t)\sigma_D^y]\} - \sin(\omega_d t)[\cos(\eta t)\sigma_D^y + \sin(\eta t)\sigma_D^x]) \\ \times [\cos(\omega_T t)\sigma_T^x - \sin(\omega_T t)\sigma_T^y], \quad (6)$$

where J_r is the resonator-mediated coupling strength between qubits D and T . We will utilize a cross-resonance interaction that results from driving the DQD energy levels in resonance with the transition frequency of qubit T , $\omega_d = \omega_T$. For sufficiently small resonator-mediated interaction strength, $J_r \ll \eta$, the rotating wave approximation can be applied again to discard rapidly oscillating terms in Eq. (6) and arrive at a Hamiltonian of the form $H_{\text{QF}} \approx -(1/2)\tilde{J}_r\sigma_D^z\sigma_T^x$, with the ZX coupling coefficient $\tilde{J}_r = J_r \sin(\chi) = J_r \Omega_{\text{eff}}^x/\eta$. Evolution under this Hamiltonian for time t_g with $J_r t_g = \pi/2$ with local operations on the T and D qubits as $U_{\text{local}} = \exp(i\frac{\pi}{4})\exp(-i\frac{\pi}{4}I_D \otimes \sigma_T^x)\exp(-i\frac{\pi}{4}\sigma_D^z \otimes I_T)$ corresponds to a CNOT gate between the qubits.

We select the transition frequencies of the qubits to be well detuned such that the two-qubit coherent interactions are suppressed without the microwave drive applied. Also, in tunnel-coupled QDs, the effect of charge noise can be intrinsically mitigated by running the device at the sweet spot or symmetric operation point, where the exchange coupling is first-order insensitive to the charge noise [65–67]. Here, since the entanglement is induced only during the pulse time (with rectangular profile here), the base value of energy level detunings for the DQD and TQD is conveniently chosen to coincide with the sweet spot $\epsilon_T = \epsilon_D = 0$ to suppress the charge noise at first order.

Figure 4(a) shows the cross-resonance CNOT gate fidelity between qubits D and T and local operations on qubit 3 as a function of time for different values of the tunnel coupling to the spectator qubit. The figure also shows the sensitivity of the gate fidelity to the frequency of the applied microwave drive, in the absence of the spectator qubit. We now explain these results in detail.

The fidelity is calculated by solving the Schrödinger equation for the full system [Eq. (1)] with the resonator mode truncated to three photonic states, and then projecting the unitary evolution onto the three-qubit logical subspace. The maximum CNOT gate fidelity in the absence of the spectator qubit, i.e., $|t_{T23}|/h = 0.0$ GHz, is 0.9829, achieved for the gate duration of $t_g = 323.6$ ns. The unitarity of the evolution in the computational subspace during the gate varies between 93.34% and 100%, which is mainly due to the leakage out of the subspace to the photon-populated resonator states

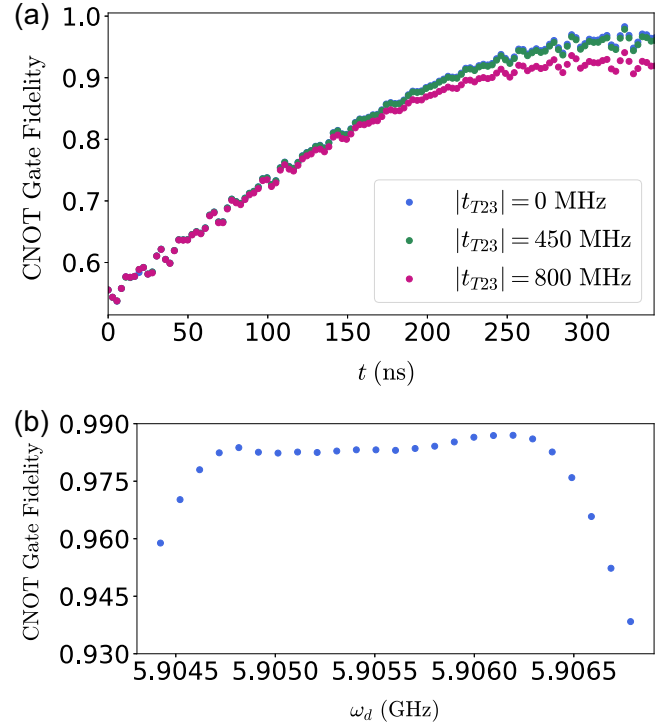


FIG. 4. (a) Cross-resonance CNOT gate fidelity between qubits D and T vs time, optimized over local operations on all qubits at each time step. Parameters are set at $\omega_r/2\pi = 6$ GHz, $\omega_D^z/2\pi = 5.94$ GHz, $\omega_D^x/2\pi = 5.96$ GHz, $\omega_3^z/2\pi = 5.8$ GHz, $|t_D|/h = |t_{T12}|/h = 3.5$ GHz, $t_{T23}/h = 0, 0.45, 0.8$ GHz, $g_T^x/2\pi = g_D^x/2\pi = 200$ MHz, $g_D^{AC}/2\pi = g_T^{AC}/2\pi = 50$ MHz, $\epsilon_D = \epsilon_T = 0$, $\epsilon_{T3}/h = -300$ GHz, $U_{T1}/h = U_{T2}/h = U_{T3}/h = 2.5$ THz. The microwave drive frequency is set to $\omega_d = \omega_T$ for cross-resonance operation. The microwave drive amplitude Ω_D is set based on $\Omega_{\text{eff}}^x/2\pi = 20$ MHz. (b) Robustness of the gate fidelity to the cross-resonance microwave drive frequency.

during the gate and is ultimately responsible for the remaining infidelity.

In principle, by increasing the barrier height between the neighboring dots, it is possible to lower the exchange strength J_e/h and nearly isolate the neighboring qubits. However, in practice, there is a limit to such isolation, resulting in residual exchange interactions in the range of a few tens of kHz to a few hundred kHz [9,13,30]. We examine the effect of such residual coupling, i.e., the presence of a spectator qubit, on the fidelity of long-range entangling gate operations.

We consider nonzero tunnel coupling strengths of $|t_{T23}|/h = 450$ MHz and 800 MHz, in Eq. (1). Starting from the Hubbard model for two neighboring dots with detuning ϵ and tunnel coupling t_c and considering conditions of $|\epsilon| < U$ and $|t_c| \ll U \pm \epsilon$, the low-energy hybridized singlet and triplet states are separated by $J = \frac{4Ut_c^2}{U^2 - \epsilon^2} + O(\frac{t_c^3}{(U \pm \epsilon)^3})$, which is the Heisenberg exchange coupling strength [3,73]. Therefore, the nonzero tunnel couplings translate to the residual coupling strength to the spectator qubit of $J_e/h = 328.7$ kHz and 1.039 MHz, resulting in the maximum gate fidelity dropping to 0.9776 and 0.9408, respectively.

Note that the simulated residual tunnel couplings are chosen such that clear gate fidelity degradations may be observed, while recent experimental efforts report the ability to reduce the residual exchange couplings down to a T_2 limit of $J_e/h \sim 10$ kHz [13], which would practically cause negligible fidelity degradations, much closer to the blue curve in Fig. 4(a). Hence, we can conclude that the presence of the third qubit would have a negligible effect on the cross-resonance CNOT gate, and increasing the barrier gate voltage between the second and third dots of the TQD module efficiently isolates the subspace of the T and D qubits.

As mentioned, the cross-resonance approach relies on matching the frequency of the applied drive to the transition frequency of the other qubit. Next, we numerically examine the robustness of the gate performance to this matching condition [Fig. 4(b)]. For each drive frequency, the gate duration is adapted to give the highest fidelity. It can be seen that with the commonly realized frequency resolution of signal generators, securing a cross-resonance operation should not be an issue.

B. Effect of charge noise on cross-resonance CNOT gates

The main source of qubit decoherence greatly depends on the details of the device fabrication even in isotopically enriched ^{28}Si . A key observation has been that for thin (~ 5 nm) quantum wells such as single-layer etch-defined gate electrode devices, without magnetic field gradients, the hyperfine effect from magnetic nuclei limits the coherence time [8], while for thicker (~ 30 – 50 nm) quantum wells with micromagnets fabricated on top of the device, similar to our platform, isotopic purification of the semiconductor leaves charge noise as the main source of decoherence [12,20,64]. Specifically, in $^{28}\text{Si}/\text{SiGe}$ with extrinsic spin–electric-coupling fields applied, studying rapid spin rotations showed that the dephasing is primarily caused by charge noise and not magnetic hyperfine noise, especially since the movement of spins through local magnetic field gradients, e.g., in EDSR, makes the qubits further susceptible to electrical fluctuations [12,20].

In view of this, next, we computationally study the effect of the charge noise on the cross-resonance CNOT gate fidelity through a sampling technique. See Appendix C for the details of the numerical simulations modeling the effect of the quasistatic charge noise in our studies. Figure 5 shows the infidelity of the cross-resonance CNOT gate versus the standard deviation of the detuning charge noise. For each value of the noise amplitude, a hundred sets of samples were taken from the Gaussian distributions.

Here, we have assumed that the qubits and resonator modes are well isolated from any bosonic bath, resulting in negligible qubit relaxation time dynamics and cavity decay rates. In the case of qubits coupled to a cavity, the Purcell effect from the resonator can impact the performance of the qubit and is thus important to consider. In this case, the decay of the qubit into the cavity mode may contribute to the total qubit decay rate. Specifically, in the case of a qubit that is coupled, with a coupling strength g_s , to a resonator with a photon decay rate of κ , the Purcell effect contributes an additional decay rate for the qubit of $\gamma_\kappa = g_s^2 \frac{\kappa}{\Delta^2 + (\kappa/2)^2}$, with the spin qubit-cavity detuning Δ . The effective spin-photon coupling rate achieved through

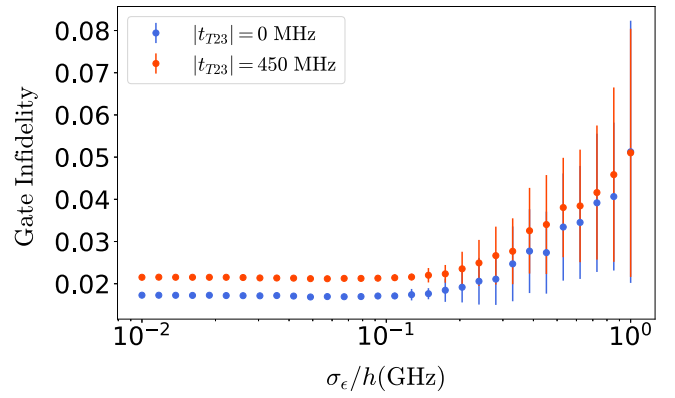


FIG. 5. Cross-resonance CNOT gate infidelity between qubits D and T vs quasistatic charge noise amplitude, optimized over local operations on all qubits at each time step. Parameters are set at $\sigma_{t_D} = \sigma_{t_{Tij}} = \sigma_{\epsilon_i}/200 = \sigma_{\epsilon_{T3}}/200$, $\omega_r/2\pi = 6$ GHz, $\omega_T^z/2\pi = 5.94$ GHz, $\omega_D^z/2\pi = 5.96$ GHz, $\omega_3^z/2\pi = 5.8$ GHz, $|t_D/2\pi| = |t_{T12}|/h = 3.5$ GHz, $|t_{T23}|/h = 0, 0.45$ GHz, $g_T^x/2\pi = g_D^x/2\pi = 200$ MHz, $g_D^A = g_T^A/2\pi = 50$ MHz, $\epsilon_D = \epsilon_T = 0$, $\epsilon_{T3}/h = -300$ GHz, $U_{T1}/h = U_{T2}/h = U_{T3}/h = 2.5$ THz. The microwave drive frequency is set to $\omega_d = \omega_T$ for cross-resonance operation, and the amplitude Ω_D is based on $\Omega_{\text{eff}}^x/2\pi = 20$ MHz. A hundred sets of samples per point from the Gaussian distribution for each noise parameter were taken, with dots showing the average gate infidelity and error bars showing the standard deviation of the infidelities.

electric-dipole interaction with spin-charge hybridized states is proportional to the charge coupling rate g_c and the dipole transition matrix element d_{ij} through $g_s = g_c|d_{ij}|$. With the third qubit isolated through $t_{T23} = 0$, the spin-charge hybridization results in low-energy eigenstates of the following form: $|0\rangle \simeq |-, \downarrow\rangle$, $|1\rangle = \cos \frac{\Phi}{2} |-, \uparrow\rangle + \sin \frac{\Phi}{2} |+, \downarrow\rangle$, $|2\rangle = \sin \frac{\Phi}{2} |-, \uparrow\rangle - \cos \frac{\Phi}{2} |+, \downarrow\rangle$, and $|3\rangle \simeq |+, \uparrow\rangle$. Here, Φ is the spin-orbit mixing angle $\Phi = \arctan \frac{B_z}{2t_c - B_z}$ [$\Phi \in (0, \pi)$] [44]. Accordingly, for the primarily spinlike transition between $|0\rangle$ and $|1\rangle$, the dipole transition matrix element is $d_{01} \simeq -\cos \theta' \sin \frac{\Phi}{2}$ with $\theta' = \arctan \frac{\epsilon}{2t_c}$. For the parameters of the cross-resonance CNOT gate with an isolated spectator, this leads to the effective spin-photon coupling rates of $g_s/2\pi \approx 8.97$ MHz and ≈ 9.13 MHz on the TQD and DQD sides, respectively. These values are within the range of the experimentally observed spin-photon couplings in the strong-coupling regime. In our theoretical and numerical studies, the resonator is considered ideal, with no photon loss or equivalently decay rate. However, a resonator with a finite quality factor may be realized in experimental cases. Considering a practical quality factor of $Q = 5000$, corresponding to a photon decay rate of $\kappa/(2\pi) = \omega_r/2\pi Q = 1.2$ MHz for $\omega_r/2\pi = 6$ GHz, the added Purcell decay rate of the encoded qubit in the TQD module with $|\Delta|/(2\pi) \approx 94.4$ MHz can be approximated as $\gamma_\kappa/(2\pi) \approx 0.011$ MHz. In the DQD module, the corresponding values are $|\Delta|/(2\pi) \approx 75.36$ MHz and $\gamma_\kappa/(2\pi) \approx 0.018$ MHz. Thus, considering the level of charge noise in practical devices and the corresponding spin decoherence rates, we can safely ignore the Purcell effect on the decay of the encoded qubits.

Our analysis (see Fig. 5) shows that charge noise levels smaller than 100 MHz have a negligible effect on the gate

fidelity, in the presence or absence of the spectator qubit. On the other hand, for larger values of the noise amplitude, the charge noise limits the fidelity of the gate and eventually dominates the infidelity due to the spectator qubit at a noise strength of 1 GHz. The level of charge noise in a given experiment highly depends on the properties of the processor and the details of the experiment. Yet, recent experiments on devices with similar geometries report charge noise values that are regularly within the left-half side of the plot [12,47,74–76], in the region where the infidelity is unperturbed by the noise. Therefore, we do not expect charge noise to have major deleterious effects on the performance of the resonator-mediated cross-resonance CNOT gates in comparison to the infidelities induced by leakage.

V. CONCLUSIONS

We examined multiqubit operations in modular semiconductor QD spin qubit systems with long-range interactions mediated by superconducting resonators. We presented and analyzed a three-qubit silicon QD-based system with both delocalized and confined electrons in a TQD subsystem and a delocalized electron in a DQD subsystem, where both the TQD and DQD are capacitively coupled to a single resonator mode. We demonstrated that the dynamics of the three-qubit system can be accurately modeled via single- and two-body terms with the anticipated structure of resonator-mediated coupling between distant qubits and exchange coupling between qubits in TQD, even though one of the qubits is delocalized, together with some small residual couplings. We studied short-range fast adiabatic CZ gates, realized by pulsing on exchange couplings, and obtained high fidelities by moving to the regime where the resonator-mediated interactions are suppressed, isolating the spectator qubit. Although incoherent noise sources favor shorter gate times, we showed that for experimentally realistic parameters, nonadiabatic errors may

be a limiting factor in reaching such faster operations and in maintaining high fidelities unless signal processing techniques are employed to reach stable operation points. We further investigated the competing effect of spectator-associated errors and the nonadiabatic errors for this case. We also investigated the performance of resonator-mediated CNOT gates that utilize a cross-resonance scheme and showed that leakage effects are the limiting factor rather than charge noise. Our results constitute an important step toward designing large QD spin qubit processors based on resonator-coupled modules containing multiple qubits.

ACKNOWLEDGMENTS

This work is supported by the National Science Foundation (Grant No. 2137776) and by the U.S. Army Research Office (Grant No. W911NF-23-1-0115).

APPENDIX A: ENCODED SUBSPACE AND THE EFFECTIVE HAMILTONIAN DERIVATION

In this Appendix, we analytically derive an effective Hamiltonian for the dynamics of the low-energy subspace of the three-qubit QD system, starting from the theoretical description of the full system, and present the relevant parameters. Without loss of generality, the average magnetic field in dots 1 and 2 of both the TQD and DQD modules is along the z axis and the magnetic field gradient is purely transversal and along the x axis. Here the electron gas is extended in the yz plane. Following these conditions, starting from the total Hamiltonian of Eq. (1), we can apply a Schrieffer-Wolff transformation [62] and trace out the doubly occupied states to arrive at the following Hamiltonian structure in terms of Pauli operators defined for the spin and orbital degrees of freedom in the DQD and TQD modules:

$$\begin{aligned}
 \hat{H}_{\text{tot}} &= \hat{H}_r + \hat{H}_{\text{DQD}} + \hat{H}_{\text{TQD}} + \hat{H}_{\text{int}}, \\
 \hat{H}_r &= \omega_r a^\dagger a, \\
 \hat{H}_{\text{DQD}} &= \frac{1}{2} \epsilon_D \tilde{\tau}_D^z - t_D \tilde{\tau}_D^x + \frac{1}{2} \omega_D^z \tilde{\sigma}_D^z + g_D^x \tilde{\tau}_D^z \tilde{\sigma}_D^x, \\
 \hat{H}_{\text{TQD}} &= \frac{1}{2} \epsilon_T \tilde{\tau}_T^z - (t_T \tilde{\tau}_T^+ + \text{H.c.}) + \frac{1}{2} \omega_T^z \tilde{\sigma}_T^z + g_T^x \tilde{\tau}_T^z \tilde{\sigma}_T^x + \frac{1}{2} \vec{B}_{T3} \cdot \vec{\sigma}_3 + \frac{1}{4} (J_0 + (J_\perp \tilde{\tau}_T^+ + \text{H.c.}) + J_z \tilde{\tau}_T^z) \tilde{\sigma}_T \cdot \vec{\sigma}_3, \\
 \hat{H}_{\text{int}} &= (a^\dagger + a) (g_D^{\text{AC}} \tilde{\tau}_D^z + g_T^{\text{AC}} \tilde{\tau}_T^z),
 \end{aligned} \tag{A1}$$

in which we have defined

$$\begin{aligned}
 \epsilon_D &= \epsilon_{D1} - \epsilon_{D2}, \\
 \omega_D^z &= \frac{1}{2} (\vec{B}_{D1} + \vec{B}_{D2}), \\
 g_D^x &= \frac{1}{4} (\vec{B}_{D1} - \vec{B}_{D2}), \\
 \epsilon_T &= \epsilon_{T1} + V_{T31} - \epsilon_{T2} - V_{T23} + \frac{1}{2} t_{T23}^2 \left(\frac{1}{U_{T2} - V_{T23} + \epsilon_{T2} - \epsilon_{T3}} + \frac{1}{U_{T3} - V_{T23} - \epsilon_{T2} + \epsilon_{T3}} + \frac{2}{V_{T31} - V_{T12} - \epsilon_{T2} + \epsilon_{T3}} \right) \\
 &\quad - \frac{1}{2} |t_{T31}|^2 \left(\frac{1}{U_{T1} - V_{T31} + \epsilon_{T1} - \epsilon_{T3}} + \frac{1}{U_{T3} - V_{T31} - \epsilon_{T1} + \epsilon_{T3}} + \frac{2}{V_{T23} - V_{T12} - \epsilon_{T1} + \epsilon_{T3}} \right),
 \end{aligned}$$

$$\begin{aligned}
t_T &= t_{T12} + \frac{1}{4} t_{T23} t_{T31} \left(\frac{1}{U_{T3} - V_{T23} - \epsilon_{T2} + \epsilon_{T3}} + \frac{1}{U_{T3} - V_{T31} - \epsilon_{T1} + \epsilon_{T3}} \right. \\
&\quad \left. + \frac{1}{V_{T23} - V_{T12} - \epsilon_{T1} + \epsilon_{T3}} + \frac{1}{V_{T31} - V_{T12} - \epsilon_{T2} + \epsilon_{T3}} \right), \\
\omega_T^z &= \frac{1}{2} (\bar{B}_{T1} + \bar{B}_{T2}), \\
g_T^x &= \frac{1}{4} (\bar{B}_{T1} - \bar{B}_{T2}), \\
J_0 &= |t_{T31}|^2 \left(\frac{1}{U_{T1} - V_{T31} + \epsilon_{T1} - \epsilon_{T3}} + \frac{1}{U_{T3} - V_{T31} - \epsilon_{T1} + \epsilon_{T3}} \right) \\
&\quad + t_{T23}^2 \left(\frac{1}{U_{T2} - V_{T23} + \epsilon_{T2} - \epsilon_{T3}} + \frac{1}{U_{T3} - V_{T23} - \epsilon_{T2} + \epsilon_{T3}} \right), \\
J_\perp &= t_{T23} t_{T31} \left(\frac{1}{U_{T3} - V_{T23} - \epsilon_{T2} + \epsilon_{T3}} + \frac{1}{U_{T3} - V_{T31} - \epsilon_{T1} + \epsilon_{T3}} + \frac{1}{V_{T12} - V_{T23} + \epsilon_{T1} - \epsilon_{T3}} + \frac{1}{V_{T12} - V_{T31} + \epsilon_{T2} - \epsilon_{T3}} \right), \\
J_z &= |t_{T31}|^2 \left(\frac{1}{U_{T1} - V_{T31} + \epsilon_{T1} - \epsilon_{T3}} + \frac{1}{U_{T3} - V_{T31} - \epsilon_{T1} + \epsilon_{T3}} \right) \\
&\quad - t_{T23}^2 \left(\frac{1}{U_{T2} - V_{T23} + \epsilon_{T2} - \epsilon_{T3}} + \frac{1}{U_{T3} - V_{T23} - \epsilon_{T2} + \epsilon_{T3}} \right), \tag{A2}
\end{aligned}$$

with the spin and orbital single-qubit j th Pauli operators for the delocalized electrons in module i labeled as $\tilde{\sigma}_i^j$ and $\tilde{\tau}_i^j$, respectively. $\tilde{\sigma}_3^j$ are the spin Pauli operators of the electron localized in the third dot of the TQD module. Capacitive resonator coupling and interdot coupling strengths are small enough compared to the energy differences of the Hamiltonian that their effect can be considered perturbatively, with the unperturbed Hamiltonian given by

$$\begin{aligned}
\tilde{H}_0 &= \sum_{i=D,T} \left[\frac{1}{2} \epsilon_i \tilde{\tau}_i^z - (t_i \tilde{\tau}_i^+ + \text{H.c.}) + \frac{1}{2} \omega_i^z \tilde{\sigma}_i^z + g_i^x \tilde{\tau}_i^z \tilde{\sigma}_i^x \right] \\
&\quad + \frac{1}{2} \bar{B}_{T3} \cdot \vec{\sigma}_3 + \omega_r a^\dagger a. \tag{A3}
\end{aligned}$$

We start by diagonalizing the unperturbed DQD Hamiltonians, which is conducted in three steps, following a similar approach as some previous theoretical works [56,57]. In the first step, we diagonalize the single-body orbital terms with the unitary transformation U_1 defined as

$$U_1 = \prod_i \exp \left(i \frac{\phi_i}{2} \tilde{\tau}_i^z \right) \exp \left(-i \frac{\theta_i}{2} \tilde{\tau}_i^y \right), \tag{A4}$$

with parameters

$$\begin{aligned}
\phi_{i=D,T} &= \arg t_i, \\
\theta_i &= \arctan \left(\frac{-2|t_i|}{\epsilon_i} \right), \\
\omega_i^a &= \sqrt{\epsilon_i^2 + 4|t_i|^2}. \tag{A5}
\end{aligned}$$

Applying the U_1 transformation, we find

$$\begin{aligned}
U_1^\dagger \tilde{H}_0 U_1 &= \sum_{i=D,T} \left\{ \frac{1}{2} \omega_i^a \tilde{\tau}_i^z + \frac{1}{2} \omega_i^z \tilde{\sigma}_i^z \right. \\
&\quad \left. + g_i^x [\cos(\theta_i) \tilde{\tau}_i^z - \sin(\theta_i) \tilde{\tau}_i^x] \tilde{\sigma}_i^x \right\} \\
&\quad + \frac{1}{2} \bar{B}_{T3} \cdot \vec{\sigma}_3 + \omega_r a^\dagger a. \tag{A6}
\end{aligned}$$

In the second step, we diagonalize the $\tilde{\tau}_i^z \tilde{\sigma}_i^x$ and remaining single-body magnetic terms with a second unitary transformation U_2 of the form

$$U_2 = \exp \left(-i \frac{\phi_3}{2} \tilde{\sigma}_3^z \right) \exp \left(-i \frac{\alpha_3}{2} \tilde{\sigma}_3^y \right) \prod_{i=D,T} \exp \left(-i \frac{\alpha_i}{2} \tilde{\tau}_i^z \tilde{\sigma}_i^y \right), \tag{A7}$$

with parameters

$$\begin{aligned}
\phi_3 &= \arctan \left(\frac{B_{T3}^y}{B_{T3}^x} \right), \\
\alpha_{i=D,T} &= \arctan \left(\frac{2g_i^x \cos(\theta_i)}{\omega_i^z} \right), \quad \alpha_3 = \arccos \left(\frac{B_{T3}^z}{|\bar{B}_{T3}|} \right), \\
\omega_{i=D,T}' &= \sqrt{(\omega_i^z)^2 + [2g_i^x \cos(\theta_i)]^2}, \quad \omega_3^a = |\bar{B}_{T3}|, \tag{A8}
\end{aligned}$$

which transforms the Hamiltonian as follows:

$$\begin{aligned}
U_2^\dagger U_1^\dagger \tilde{H}_0 U_1 U_2 &= \sum_{i=D,T} \left[\frac{1}{2} \omega_i^a \tilde{\tau}_i^z + \frac{1}{2} \omega_i^z \tilde{\sigma}_i^z - g_i^x \sin(\theta_i) \tilde{\tau}_i^x \tilde{\sigma}_i^x \right] \\
&\quad + \frac{1}{2} \omega_3^a \tilde{\sigma}_3^z + \omega_r a^\dagger a. \tag{A9}
\end{aligned}$$

The third step is transformation U_3 in order to eliminate the remaining two-body terms, i.e., $\tilde{\tau}_i^x \tilde{\sigma}_i^x$, and fully diagonalize \tilde{H}_0 ,

$$U_3 = \prod_{i=D,T} \exp \left[-i \frac{1}{2} \left(\frac{\beta_i^+ + \beta_i^-}{2} \tilde{\tau}_i^y \tilde{\sigma}_i^x + \frac{\beta_i^+ - \beta_i^-}{2} \tilde{\tau}_i^x \tilde{\sigma}_i^y \right) \right], \quad (\text{A10})$$

with parameters

$$\begin{aligned} \omega_i^\tau \pm \omega_i^\sigma &= \sqrt{(\omega_i^a \pm \omega_i^{z'})^2 + [2g_i^x \sin(\theta_i)]^2}, \\ \beta_i^\pm &= \arctan \left(\frac{-2g_i^x \sin(\theta_i)}{\omega_i^a \pm \omega_i^{z'}} \right), \\ \beta_i &= \frac{1}{2}(\beta_i^+ + \beta_i^-). \end{aligned} \quad (\text{A11})$$

After applying all three unitary operations, the Hamiltonian is fully diagonalized, which can be equivalently summarized via transformed Pauli operators for spins and orbitals as

$$\tilde{H}_0 = \omega_r a^\dagger a + \sum_{i=D,T} \frac{1}{2} \omega_i^\tau \tau_i^z + \sum_{i=D,T,3} \frac{1}{2} \omega_i^\sigma \sigma_i^z, \quad (\text{A12})$$

with transformed Pauli operators

$$\begin{aligned} \tau_i &= U_1 U_2 U_3 \tilde{\tau}_i U_3^\dagger U_2^\dagger U_1^\dagger, \\ \sigma_i &= U_1 U_2 U_3 \tilde{\sigma}_i U_3^\dagger U_2^\dagger U_1^\dagger. \end{aligned} \quad (\text{A13})$$

Now, the total transformed system Hamiltonian is

$$\begin{aligned} \tilde{H} &= \tilde{H}_0 + \tilde{H}_I, \\ \tilde{H}_I &= \sum_{i=D,T} g_i^{AC} (a^\dagger + a) d_i + H_{\text{exch}}, \end{aligned} \quad (\text{A14})$$

where d_i are transformed dipole operators, similar to the previously studied resonator-mediated two-electron systems [57], and H_{exch} is the transformed exchange Hamiltonian:

$$\begin{aligned} d_i &= \tilde{\tau}_i^z = \frac{1}{2} [\cos(\theta_i) [\cos(\beta_i^+) + \cos(\beta_i^-)] - \sin(\theta_i) \sin(\alpha_i) [\sin(\beta_i^+) - \sin(\beta_i^-)]] \tau_i^z \\ &+ \frac{1}{2} [\cos(\theta_i) [\cos(\beta_i^+) - \cos(\beta_i^-)] - \sin(\theta_i) \sin(\alpha_i) [\sin(\beta_i^+) + \sin(\beta_i^-)]] \sigma_i^z \\ &- \frac{1}{2} [\cos(\theta_i) [\sin(\beta_i^+) + \sin(\beta_i^-)] + \sin(\theta_i) \sin(\alpha_i) [\cos(\beta_i^+) - \cos(\beta_i^-)]] \sigma_i^x \tau_i^x \\ &+ \frac{1}{2} [\cos(\theta_i) [\sin(\beta_i^+) - \sin(\beta_i^-)] + \sin(\theta_i) \sin(\alpha_i) [\cos(\beta_i^+) + \cos(\beta_i^-)]] \sigma_i^y \tau_i^y - \sin(\theta_i) \cos(\alpha_i) \cos(\beta_i) \tau_i^x \\ &- \sin(\theta_i) \cos(\alpha_i) \sin(\beta_i) \sigma_i^x \tau_i^z. \end{aligned} \quad (\text{A15})$$

Next, we apply a Schrieffer-Wolff transformation [62] to isolate the dynamics governing the low-energy subsystem to leading order, treating \tilde{H}_0 as the unperturbed Hamiltonian and \tilde{H}_I as the perturbation, under the assumption $g_i^{AC} \ll |\omega_i^\tau - \omega_r|$, $|\omega_r - \omega_i^\sigma|$, $|\omega_r - (\omega_i^\tau - \omega_i^\sigma)|$. This analytical step in combination with numerical comparison allows us to eliminate the couplings of QD modules and the resonator to leading order, as well as the coupling between the ground and excited orbital states, defining the low-energy subspace as $\langle a^\dagger a \rangle = 0$ and $\langle \tau_i^z \rangle = -1$. Eventually, this enables us to capture the dynamics of the low-energy encoded subspace with a good approximation via the effective Hamiltonian H_{eff} ,

$$\hat{H}_{\text{eff}} = \sum_{i=D,T,3} \frac{1}{2} \omega_i \sigma_i^z - J_r \sigma_D^x \sigma_T^x + e^{i\alpha_3 \sigma_3^y} e^{i\phi_3 \sigma_3^z} \left(\frac{J_e}{4} \vec{\sigma}_T \cdot \vec{\sigma}_3 + J_{ZZ} \sigma_T^z \sigma_3^z \right) e^{-i\phi_3 \sigma_3^z} e^{-i\alpha_3 \sigma_3^y}. \quad (\text{A16})$$

In this effective Hamiltonian, the parameters ϕ_3 and α_3 are defined in Eq. (A8) and the rest of the parameters are as follows:

$$\begin{aligned} \omega_{i=D,T} &= \omega_i^\sigma - 2\omega_i^\tau \frac{(g_i^{AC})^2}{\omega_r^2 - (\omega_i^\sigma)^2} [\sin(\theta_i) \cos(\alpha_i) \sin(\beta_i)]^2 \\ &+ \left(\frac{(g_i^{AC})^2}{\omega_r + \omega_i^\tau + \omega_i^\sigma} - \frac{\omega_i^\tau + \omega_i^\sigma}{2} \frac{\tilde{\Omega}_i^2}{(\omega_i^d)^2 - (\omega_i^\tau + \omega_i^\sigma)^2} \right) [\cos(\theta_i) \sin(\beta_i^+) + \sin(\theta_i) \sin(\alpha_i) \cos(\beta_i^+)]^2 \\ &+ \left(\frac{\omega_i^\tau - \omega_i^\sigma}{2} \frac{\tilde{\Omega}_i^2}{(\omega_i^d)^2 - (\omega_i^\tau - \omega_i^\sigma)^2} - \frac{(g_i^{AC})^2}{\omega_r + \omega_i^\tau - \omega_i^\sigma} \right) [\cos(\theta_i) \sin(\beta_i^-) - \sin(\theta_i) \sin(\alpha_i) \cos(\beta_i^-)]^2 \\ &+ \frac{g_i^{AC}}{\omega_r} \{ \cos(\theta_i) [\cos(\beta_i^+) - \cos(\beta_i^-)] - \sin(\theta_i) \sin(\alpha_i) [\sin(\beta_i^+) + \sin(\beta_i^-)] \} \\ &\times \sum_{j=D,T} g_j^{AC} \{ \cos(\theta_j) [\cos(\beta_j^+) + \cos(\beta_j^-)] - \sin(\theta_j) \sin(\alpha_j) [\sin(\beta_j^+) - \sin(\beta_j^-)] \}, \\ J_r &= \omega_r g_D^{AC} g_T^{AC} \sin(\theta_D) \cos(\alpha_D) \sin(\beta_D) \sin(\theta_T) \cos(\alpha_T) \sin(\beta_T) \left(\frac{1}{\omega_r^2 - (\omega_D^\sigma)^2} + \frac{1}{\omega_r^2 - (\omega_T^\sigma)^2} \right), \end{aligned}$$

$$\begin{aligned}
\omega_3 &= \omega_3^\sigma - \frac{1}{4}J_0 \cos(\alpha_T)[\cos(\beta_T^+) - \cos(\beta_T^-)], \\
J_e &= \cos\left(\frac{\beta_T^- - \beta_T^+}{2}\right) \cos(\alpha_T)J_0 - \cos(\beta_T) \cos(\alpha_T)[J_z \cos(\theta_T) + \text{Re}(J_\perp e^{-i\phi_T}) \sin(\theta_T)], \\
J_{ZZ} &= -\frac{1}{2} \sin^2\left(\frac{\beta_T}{2}\right) \cos(\alpha_T) \left[\cos\left(\frac{\beta_T^- - \beta_T^+}{2}\right)J_0 + J_z \cos(\theta_T) + \text{Re}(J_\perp e^{-i\phi_T}) \sin(\theta_T) \right].
\end{aligned} \tag{A17}$$

For the considered arrangement of the magnetic field in the TQD module (Fig. 1), $\phi_3 = 0$ and $\alpha_3 = 0$, corresponding to the effective Hamiltonian expressed in the main text [Eq. (2)]. We tested the validity of this effective Hamiltonian numerically with the results reported in Sec. II C of the main text.

APPENDIX B: FAST ADIABATIC CZ GATES BETWEEN QUBITS T AND 3 WITH PIECEWISE CONSTANT EXCHANGE PULSES

In this Appendix, we study the piecewise constant approximation of the smooth Hann window function, in the case of short-range CZ gates within the TQD module, by replacing the smooth pulses with piecewise constant functions composed of N_p segments. Note that the rectangular signal in this case corresponds to the piecewise constant function with $N_p = 1$. We numerically solve the Schrödinger equation with the full-system Hamiltonian [Eq. (1)] and the corresponding time-varying tunnel couplings $t_{T23}(t)$ and calculate the CZ gate fidelities. Similar to the results presented in the main text, we evaluate the performance of the entangling gate while considering the impact of the gate on the idle qubit (qubit D in this case). This is done such that the reported CZ gate fidelities refer to three-qubit gate fidelities relative to the block-diagonal target gate with an ideal CZ gate in one block and a single-qubit operation on the other, i.e., $U_{\text{goal}}^{\text{CZ}} = \text{CZ}_{T3} \otimes I_D$. Starting from the Hann window pulse, $J_e(t) = J_0 W_{\text{Hann}}$, with the window function $W_{\text{Hann}}(t) = \frac{1}{2}[1 - \cos(2\pi t/t_g)]$, the CZ gate is reached at $t_g = 2\pi/J_0$. The amplitudes of the piecewise constant exchange pulses are designed here such that the area under the curve for each segment of the piecewise function would be equal to that of the smooth Hann function. Figure 6 shows the temporal profile of the exchange coupling strengths, J_e , for different piecewise constant approximations of the control signals. Figures 6(a)–6(d) show exchange coupling strengths for the fast adiabatic CZ gates satisfying the synchronized evolution condition with $t_g \omega_q/2\pi = 8$ [with the same system parameters as in Fig. 3(c) of the main text]. Likewise, Figs. 6(e)–6(h) show the control signals for longer adiabatic CZ gates with $t_g = 100$ ns [with the same system parameters as in Fig. 3(d) of the main text]. Piecewise constant approximated controls with $N_p = 5, 10, 20$, and 40 segments are studied here.

Figure 7 shows the infidelity $(1 - F)$ of fast adiabatic CZ gates between qubits T and 3 along with local operations on qubit D as a function of time for different control signals and different regions of operation. Figure 7(a) shows the CZ gate infidelities for synchronization at $t_g \omega_q/2\pi = 8$, which is matched with a gate time of $t_g = 52.98$ ns for the Hann and rectangular window functions, as well as for

piecewise constant pulses. The spectator qubit coupling is $|J_r|/h = 1.68$ kHz. Similar exchange pulses but for longer CZ gate times of $t_g = 100$ ns, matching $t_g \omega_q/2\pi \approx 15.08$, result in the gate infidelities shown in Fig. 7(b). The maximum infidelities of the oscillatory infidelity functions after the CZ gate time for all cases are reported in Table I. With the pulses that match the zeros of the power spectral density function, it is possible to notably decrease the nonadiabatic error of the fast CZ gates through synchronization. This, in fact, leads to the same order of gate infidelities for the first and second rows in Table I, while the gate time is much shorter for the synchronized evolution (first row). This is wholly based on the connection between the nonadiabatic errors and the spectral profile of the pulse [see Fig. 3(e)]. For the synchronized evolution, rectangular pulses increase the infidelity by 8.7×10^{-6} , while by increasing the number of segments the infidelity gradually decreases. Eventually, for the piecewise constant pulse with $N_p = 40$ segments, the same level of fidelity as the smooth Hann pulse is reached (with 7 digits of precision reported here). A similar trend appears for the long CZ gates (second row of the table), in which by increasing the number of segments the gate infidelities decrease, and infidelities of the smooth Hann signal are reached by $N_p = 40$ segments. Note that all of the infidelities are within close proximity, as can also be seen in Fig. 7.

Synchronization is the key to reaching high fidelity for short gate times if no smooth window function is applied. Without the synchronization condition satisfied, sharp pulses lead to much higher infidelities compared to smooth Hann pulses. The third row of Table I shows the infidelities for the asynchronized evolutions with $t_g \omega_q/2\pi = 8.5$. One can see that by using piecewise constant functions with $N_p > 1$, better gate fidelities may be reached, especially if more and more segments are introduced to mimic the operation of the smooth Hann windows. Specifically, with $N_p = 20$ segments, infidelities as low as 1.838×10^{-4} are reached, which are almost identical to the infidelities for smooth Hann functions. Thus, it is important to incorporate window functions to reach high gate fidelities at short gate times, especially when access to high bandwidth pulses gets restricted due to the limited bandwidth of the system control electronics.

APPENDIX C: MODELING THE EFFECTS OF QUASISTATIC CHARGE NOISE

In this Appendix, we present the steps implemented, as part of the numerical studies, to simulate the effect of the quasistatic charge noise on the performance of the quantum gates.

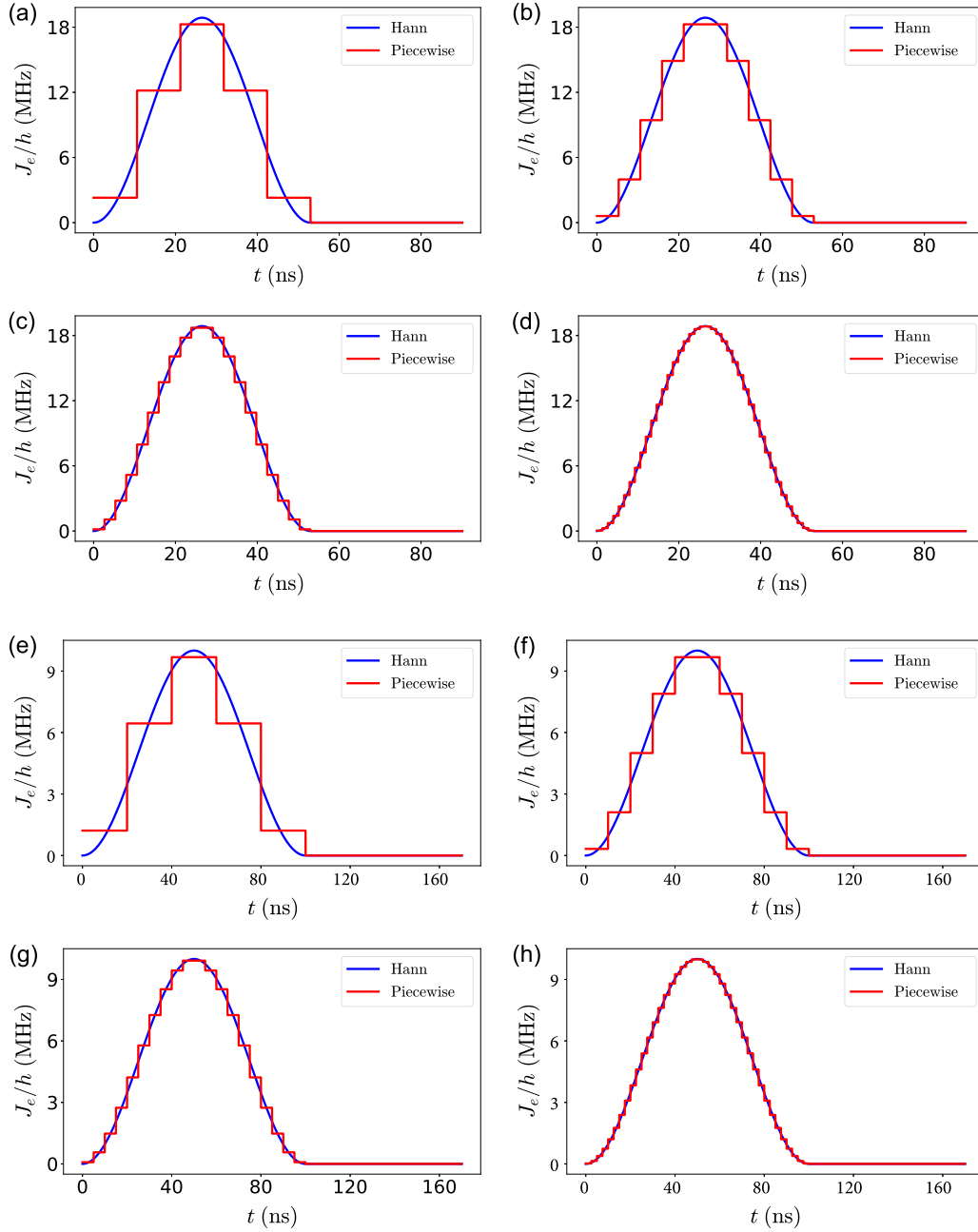


FIG. 6. Designed piecewise constant exchange coupling strengths, J_e , to realize fast adiabatic CZ gates (a)–(d) through synchronized evolution with $t_g\omega_q/2\pi = 8$ and (e)–(h) at long gate times of $t_g = 100$ ns. System parameters are the same as Figs. 3(c) and 3(d). Piecewise constant approximated exchange couplings with (a),(e) $N_p = 5$, (b),(f) $N_p = 10$, (c),(g) $N_p = 20$, and (d),(h) $N_p = 40$ segments are considered to satisfy the CZ gate evolution conditions. Piecewise constant functions are plotted on top of the smooth Hann window functions for comparison.

TABLE I. Infidelities ($1 - F$) of fast adiabatic CZ gates between qubits T and 3 along with local operations on qubit D .

CZ gate time (t_g)	Hann	Piecewise constant functions				
		Rectangular ($N_p = 1$)	$N_p = 5$	$N_p = 10$	$N_p = 20$	$N_p = 40$
52.98 ns ^a	1.836×10^{-4}	1.923×10^{-4}	1.876×10^{-4}	1.875×10^{-4}	1.840×10^{-4}	1.836×10^{-4}
100 ns	1.856×10^{-4}	2.177×10^{-4}	2.280×10^{-4}	1.864×10^{-4}	1.857×10^{-4}	1.856×10^{-4}
56.31 ns ^b	1.825×10^{-4}	1.739×10^{-3}	7.933×10^{-4}	1.098×10^{-3}	1.838×10^{-4}	1.838×10^{-4}

^aSynchronized evolution with $t_g\omega_q/2\pi = 8$.

^bAsynchronous evolution with $t_g\omega_q/2\pi = 8.5$.

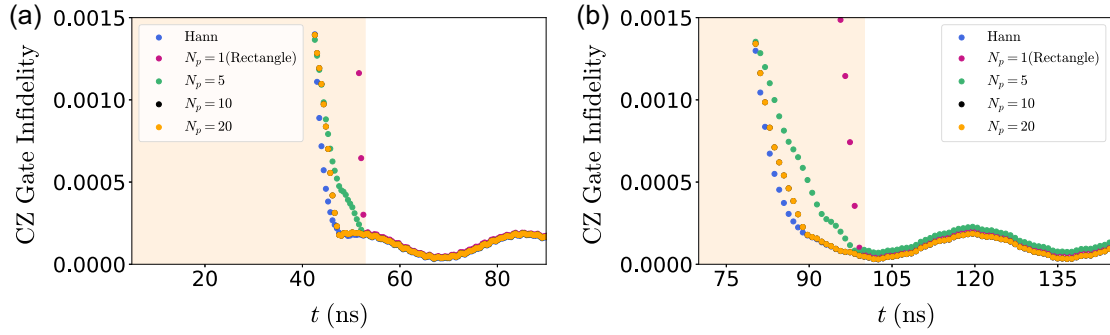


FIG. 7. Short-range CZ gate in the TQD module through fast adiabatic evolution with different control signals. (a) CZ gate infidelity for synchronized evolutions at $t_g \omega_q / 2\pi = 8$ with Hann, rectangular, and piecewise constant pulses. (b) CZ gate infidelity for a gate time of $t_g = 100$ ns with Hann, rectangular, and piecewise constant pulses. Piecewise constant approximated controls with $N_p = 5, 10, 20$, and 40 segments are considered, and gate times in (a) and (b) are shown with light-orange shadings. Additional system parameters are $\omega_r / 2\pi = 6$ GHz, $\omega_T^z / 2\pi = 5.94$ GHz, $\omega_D^z / 2\pi = 5.96$ GHz, $\omega_3^z / 2\pi = 5.8$ GHz, $|t_D|/h = |t_{12}|/h = 3.5$ GHz, $t_{T23} = t_{T23}(t)$, $g_T^z / 2\pi = g_D^z / 2\pi = 200$ MHz, $g_D^A / 2\pi = g_T^A / 2\pi = 50$ MHz, $\epsilon_{T3}/h = -300$ GHz, $U_{T1}/h = U_{T2}/h = U_{T3}/h = 2.5$ THz, and $\epsilon_T/h = \epsilon_D/h = 15$.

We model the effect of the quasistatic charge noise through a sampling technique in the simulations. This is achieved by including classical fluctuations to the elements of the Hamiltonian affected by electric fields, in particular the chemical potential of dots and the tunnel couplings. Specifically, we substitute ϵ_i with $\epsilon_i + \delta\epsilon_i$, t_D with $t_D + \delta t_D$, t_{Tij} with $t_{Tij} + \delta t_{Tij}$, and ϵ_{T3} with $\epsilon_{T3} + \delta\epsilon_{T3}$, for the detunings and the interdot tunnel couplings in the DQD and TQD modules, as well as the chemical potential of the third dot in the TQD module. Gaussian distributions are assumed for the random variables $\delta\epsilon_i$, δt_D , δt_{Tij} , and $\delta\epsilon_{T3}$ with standard deviations σ_{ϵ_i} , σ_{t_D} , $\sigma_{t_{Tij}}$, and $\sigma_{\epsilon_{T3}}$, respectively. The inclusion of these fluctuations in the dynamics of the system results in random shifts of the effective single-body and interaction parameters for different realizations of the system. For the specific case of the cross-resonance CNOT gate presented in Sec. IV, the introduction of quasistatic charge noise creates random shifts in the qubits' energy splittings, together with the effective two-qubit coupling terms in the low-energy subspace of the system. Such random fluctuations potentially limit the gate fidelities, as evident in Fig. 5.

The rate of change of the tunnel coupling with barrier gate voltage (i.e., lever arm) is typically two orders of magnitude smaller than that of the voltage-controlled detuning levels (see Refs. [77] and [78–80] for tunnel coupling and detuning control calibrations, respectively). Thus, assuming comparable levels of voltage noise in all gates, the amplitude of detuning

noise may be considered to be at least two orders of magnitude larger than the amplitude of tunnel coupling noise [65,67]. These practical considerations are applied in numerical simulations. See the caption of Fig. 5 for the parameter values.

Here we model the dephasing process by creating slow fluctuations, with Gaussian distributions, of the system's electrostatic environment (chemical potentials and tunnel barriers), capturing the impact of the interaction with the environment, while making a quasistatic approximation. Alternatively, decoherence effects can be modeled by including relevant Lindblad operators in the master equation describing the time evolution of the system density operator, in the Markovian limit. For example, in the case of two-qubit systems, Ref [58] considers phenomenological models for the Lindblad operators, capturing charge-noise and phonon relaxation effects that include low- and high-frequency noise mechanisms.

In two-qubit processors, gate sequences have been devised to suppress the sensitivity of two-qubit entangling gates to similar quasistatic charge-noise effects [57]. For the three-qubit processors considered here and in cases where the existence of high levels of charge noise combined with the effects of the spectator qubit may cause adverse effects on the gate fidelities (see Sec. IV for a discussion), such noise-suppression techniques need to be expanded to address decoherence effects. Devising such protocols for three-qubit processes is beyond the scope of this work and is left to future studies.

- [1] D. Loss and D. P. DiVincenzo, Quantum computation with quantum dots, *Phys. Rev. A* **57**, 120 (1998).
- [2] N. P. de Leon, K. M. Itoh, D. Kim, K. K. Mehta, T. E. Northup, H. Paik, B. Palmer, N. Samarth, S. Sangtawesin, and D. W. Steuerman, Materials challenges and opportunities for quantum computing hardware, *Science* **372**, eabb2823 (2021).
- [3] G. Burkard, T. D. Ladd, J. M. Nichol, A. Pan, and J. R. Petta, Semiconductor spin qubits, *Rev. Mod. Phys.* **95**, 025003 (2023).

- [4] M. Veldhorst, H. Eenink, C.-H. Yang, and A. S. Dzurak, Silicon CMOS architecture for a spin-based quantum computer, *Nat. Commun.* **8**, 1766 (2017).
- [5] W. Ha, S. D. Ha, M. D. Choi, Y. Tang, A. E. Schmitz, M. P. Levendoff, K. Lee, J. M. Chappell, T. S. Adams, D. R. Hulbert *et al.*, A flexible design platform for Si/SiGe exchange-only qubits with low disorder, *Nano Lett.* **22**, 1443 (2022).
- [6] A. M. J. Zwerver, T. Krähenmann, T. F. Watson, L. Lampert, H. C. George, R. Pillarisetty, S. A. Bojarski, P. Amin, S. V.

- Amitonov, J. M. Boter, R. Caudillo, D. Correias-Serrano, J. P. Dehollain, G. Droulers, E. M. Henry, R. Kotlyar, M. Lodari, F. Lüthi, D. J. Michalak, B. K. Mueller *et al.*, Qubits made by advanced semiconductor manufacturing, *Nat. Electron.* **5**, 184 (2022).
- [7] J. Z. Blumoff, A. S. Pan, T. E. Keating, R. W. Andrews, D. W. Barnes, T. L. Brecht, E. T. Croke, L. E. Euliss, J. A. Fast, C. A. C. Jackson *et al.*, Fast and high-fidelity state preparation and measurement in triple-quantum-dot spin qubits, *PRX Quantum* **3**, 010352 (2022).
- [8] A. J. Weinstein, M. D. Reed, A. M. Jones, R. W. Andrews, D. Barnes, J. Z. Blumoff, L. E. Euliss, K. Eng, B. H. Fong, S. D. Ha *et al.*, Universal logic with encoded spin qubits in silicon, *Nature (London)* **615**, 817 (2023).
- [9] X. Xue, M. Russ, N. Samkharadze, B. Undseth, A. Sammak, G. Scappucci, and L. M. Vandersypen, Quantum logic with spin qubits crossing the surface code threshold, *Nature (London)* **601**, 343 (2022).
- [10] K. Takeda, A. Noiri, T. Nakajima, J. Yoneda, T. Kobayashi, and S. Tarucha, Quantum tomography of an entangled three-qubit state in silicon, *Nat. Nanotechnol.* **16**, 965 (2021).
- [11] C. Yang, K. Chan, R. Harper, W. Huang, T. Evans, J. Hwang, B. Hensen, A. Laucht, T. Tanttu, F. Hudson *et al.*, Silicon qubit fidelities approaching incoherent noise limits via pulse engineering, *Nat. Electron.* **2**, 151 (2019).
- [12] J. Yoneda, K. Takeda, T. Otsuka, T. Nakajima, M. R. Delbecq, G. Allison, T. Honda, T. Kodera, S. Oda, Y. Hoshi *et al.*, A quantum-dot spin qubit with coherence limited by charge noise and fidelity higher than 99.9%, *Nat. Nanotechnol.* **13**, 102 (2018).
- [13] A. R. Mills, C. R. Guinn, M. J. Gullans, A. J. Sigillito, M. M. Feldman, E. Nielsen, and J. R. Petta, Two-qubit silicon quantum processor with operation fidelity exceeding 99%, *Sci. Adv.* **8**, eabn5130 (2022).
- [14] T. Tanttu, W. H. Lim, J. Y. Huang, N. D. Stuyck, W. Gilbert, R. Y. Su, M. Feng, J. D. Cifuentes, A. E. Seedhouse, S. K. Seritan *et al.*, Assessment of error variation in high-fidelity two-qubit gates in silicon, *Nat. Phys.* (2024), doi:10.1038/s41567-024-02614-w.
- [15] A. G. Fowler, M. Mariantoni, J. M. Martinis, and A. N. Cleland, Surface codes: Towards practical large-scale quantum computation, *Phys. Rev. A* **86**, 032324 (2012).
- [16] A. Noiri, K. Takeda, T. Nakajima, T. Kobayashi, A. Sammak, G. Scappucci, and S. Tarucha, Fast universal quantum gate above the fault-tolerance threshold in silicon, *Nature (London)* **601**, 338 (2022).
- [17] C. H. Yang, R. Leon, J. Hwang, A. Saraiva, T. Tanttu, W. Huang, J. Camirand Lemyre, K. W. Chan, K. Tan, F. E. Hudson *et al.*, Operation of a silicon quantum processor unit cell above one kelvin, *Nature (London)* **580**, 350 (2020).
- [18] L. Petit, M. Russ, G. H. Eenink, W. I. Lawrie, J. S. Clarke, L. M. Vandersypen, and M. Veldhorst, Design and integration of single-qubit rotations and two-qubit gates in silicon above one kelvin, *Commun. Mater.* **3**, 82 (2022).
- [19] M. Pioro-Ladriere, T. Obata, Y. Tokura, Y.-S. Shin, T. Kubo, K. Yoshida, T. Taniyama, and S. Tarucha, Electrically driven single-electron spin resonance in a slanting zeeman field, *Nat. Phys.* **4**, 776 (2008).
- [20] E. Kawakami, T. Jullien, P. Scarlino, D. R. Ward, D. E. Savage, M. G. Lagally, V. V. Dobrovitski, M. Friesen, S. N. Coppersmith, M. A. Eriksson *et al.*, Gate fidelity and coherence of an electron spin in an Si/SiGe quantum dot with micromagnet, *Proc. Natl. Acad. Sci. USA* **113**, 11738 (2016).
- [21] X. Croot, X. Mi, S. Putz, M. Benito, F. Borjans, G. Burkard, and J. R. Petta, Flopping-mode electric dipole spin resonance, *Phys. Rev. Res.* **2**, 012006(R) (2020).
- [22] D. M. Zajac, A. J. Sigillito, M. Russ, F. Borjans, J. M. Taylor, G. Burkard, and J. R. Petta, Resonantly driven CNOT gate for electron spins, *Science* **359**, 439 (2018).
- [23] W. Huang, C. Yang, K. Chan, T. Tanttu, B. Hensen, R. Leon, M. Fogarty, J. Hwang, F. Hudson, K. M. Itoh *et al.*, Fidelity benchmarks for two-qubit gates in silicon, *Nature (London)* **569**, 532 (2019).
- [24] T. Watson, S. Philips, E. Kawakami, D. Ward, P. Scarlino, M. Veldhorst, D. Savage, M. Lagally, M. Friesen, S. Coppersmith *et al.*, A programmable two-qubit quantum processor in silicon, *Nature (London)* **555**, 633 (2018).
- [25] J. R. Petta, A. C. Johnson, J. M. Taylor, E. A. Laird, A. Yacoby, M. D. Lukin, C. M. Marcus, M. P. Hanson, and A. C. Gossard, Coherent manipulation of coupled electron spins in semiconductor quantum dots, *Science* **309**, 2180 (2005).
- [26] K. Nowack, M. Shafiei, M. Laforest, G. Prawiroatmodjo, L. Schreiber, C. Reichl, W. Wegscheider, and L. Vandersypen, Single-shot correlations and two-qubit gate of solid-state spins, *Science* **333**, 1269 (2011).
- [27] Y. P. Kandel, H. Qiao, S. Fallahi, G. C. Gardner, M. J. Manfra, and J. M. Nichol, Coherent spin-state transfer via Heisenberg exchange, *Nature (London)* **573**, 553 (2019).
- [28] K. Takeda, A. Noiri, J. Yoneda, T. Nakajima, and S. Tarucha, Resonantly driven singlet-triplet spin qubit in silicon, *Phys. Rev. Lett.* **124**, 117701 (2020).
- [29] A. Sigillito, M. Gullans, L. Edge, M. Borselli, and J. Petta, Coherent transfer of quantum information in a silicon double quantum dot using resonant SWAP gates, *npj Quantum Inf.* **5**, 110 (2019).
- [30] K. Takeda, A. Noiri, T. Nakajima, T. Kobayashi, and S. Tarucha, Quantum error correction with silicon spin qubits, *Nature (London)* **608**, 682 (2022).
- [31] M. Veldhorst, C. Yang, J. Hwang, W. Huang, J. Dehollain, J. Muhonen, S. Simmons, A. Laucht, F. Hudson, K. M. Itoh *et al.*, A two-qubit logic gate in silicon, *Nature (London)* **526**, 410 (2015).
- [32] X. Xue, T. F. Watson, J. Helsen, D. R. Ward, D. E. Savage, M. G. Lagally, S. N. Coppersmith, M. A. Eriksson, S. Wehner, and L. M. K. Vandersypen, Benchmarking gate fidelities in a Si/SiGe two-qubit device, *Phys. Rev. X* **9**, 021011 (2019).
- [33] S. G. Philips, M. T. Mądzik, S. V. Amitonov, S. L. de Snoo, M. Russ, N. Kalhor, C. Volk, W. I. Lawrie, D. Brousse, L. Trypuzen *et al.*, Universal control of a six-qubit quantum processor in silicon, *Nature (London)* **609**, 919 (2022).
- [34] L. Vandersypen, H. Bluhm, J. Clarke, A. Dzurak, R. Ishihara, A. Morello, D. Reilly, L. Schreiber, and M. Veldhorst, Interfacing spin qubits in quantum dots and donors—Hot, dense, and coherent, *npj Quantum Inf.* **3**, 34 (2017).
- [35] H. Jnane, B. Undseth, Z. Cai, S. C. Benjamin, and B. Koczor, Multicore quantum computing, *Phys. Rev. Appl.* **18**, 044064 (2022).
- [36] A. R. Mills, D. M. Zajac, M. J. Gullans, F. J. Schupp, T. M. Hazard, and J. R. Petta, Shuttling a single charge across a

- one-dimensional array of silicon quantum dots, *Nat. Commun.* **10**, 1063 (2019).
- [37] A. Noiri, K. Takeda, T. Nakajima, T. Kobayashi, A. Sammak, G. Scappucci, and S. Tarucha, A shuttling-based two-qubit logic gate for linking distant silicon quantum processors, *Nat. Commun.* **13**, 5740 (2022).
- [38] M. A. Sillanpää, J. I. Park, and R. W. Simmonds, Coherent quantum state storage and transfer between two phase qubits via a resonant cavity, *Nature (London)* **449**, 438 (2007).
- [39] J. Majer, J. Chow, J. Gambetta, J. Koch, B. Johnson, J. Schreier, L. Frunzio, D. Schuster, A. A. Houck, A. Wallraff *et al.*, Coupling superconducting qubits via a cavity bus, *Nature (London)* **449**, 443 (2007).
- [40] D. J. Egger and F. K. Wilhelm, Optimized controlled-z gates for two superconducting qubits coupled through a resonator, *Supercond. Sci. Technol.* **27**, 014001 (2014).
- [41] F. Borjans, X. Croot, X. Mi, M. Gullans, and J. Petta, Resonant microwave-mediated interactions between distant electron spins, *Nature (London)* **577**, 195 (2020).
- [42] P. Harvey-Collard, J. Dijkema, G. Zheng, A. Sammak, G. Scappucci, and L. M. K. Vandersypen, Coherent spin-spin coupling mediated by virtual microwave photons, *Phys. Rev. X* **12**, 021026 (2022).
- [43] X. Hu, Y.-X. Liu, and F. Nori, Strong coupling of a spin qubit to a superconducting stripline cavity, *Phys. Rev. B* **86**, 035314 (2012).
- [44] M. Benito, X. Mi, J. M. Taylor, J. R. Petta, and G. Burkard, Input-output theory for spin-photon coupling in Si double quantum dots, *Phys. Rev. B* **96**, 235434 (2017).
- [45] X. Mi, J. Cady, D. Zajac, P. Deelman, and J. R. Petta, Strong coupling of a single electron in silicon to a microwave photon, *Science* **355**, 156 (2017).
- [46] N. Samkharadze, G. Zheng, N. Kalhor, D. Brousse, A. Sammak, U. Mendes, A. Blais, G. Scappucci, and L. Vandersypen, Strong spin-photon coupling in silicon, *Science* **359**, 1123 (2018).
- [47] X. Mi, M. Benito, S. Putz, D. M. Zajac, J. M. Taylor, G. Burkard, and J. R. Petta, A coherent spin-photon interface in silicon, *Nature (London)* **555**, 599 (2018).
- [48] A. J. Landig, J. V. Koski, P. Scarlino, U. Mendes, A. Blais, C. Reichl, W. Wegscheider, A. Wallraff, K. Ensslin, and T. Ihn, Coherent spin-photon coupling using a resonant exchange qubit, *Nature (London)* **560**, 179 (2018).
- [49] J. Dijkema, X. Xue, P. Harvey-Collard, M. Rimbach-Russ, S. L. de Snoo, G. Zheng, A. Sammak, G. Scappucci, and L. M. Vandersypen, Two-qubit logic between distant spins in silicon, *arXiv:2310.16805*.
- [50] E. J. Connors, J. J. Nelson, H. Qiao, L. F. Edge, and J. M. Nichol, Low-frequency charge noise in Si/SiGe quantum dots, *Phys. Rev. B* **100**, 165305 (2019).
- [51] E. J. Connors, J. Nelson, L. F. Edge, and J. M. Nichol, Charge-noise spectroscopy of Si/SiGe quantum dots via dynamically-decoupled exchange oscillations, *Nat. Commun.* **13**, 940 (2022).
- [52] G. Cao, H.-O. Li, G.-D. Yu, B.-C. Wang, B.-B. Chen, X.-X. Song, M. Xiao, G.-C. Guo, H.-W. Jiang, X. Hu *et al.*, Tunable hybrid qubit in a GaAs double quantum dot, *Phys. Rev. Lett.* **116**, 086801 (2016).
- [53] A. M. Tyryshkin, S. Tojo, J. J. Morton, H. Riemann, N. V. Abrosimov, P. Becker, H.-J. Pohl, T. Schenkel, M. L. Thewalt, K. M. Itoh *et al.*, Electron spin coherence exceeding seconds in high-purity silicon, *Nat. Mater.* **11**, 143 (2012).
- [54] V. Srinivasa, J. M. Taylor, and C. Tahan, Entangling distant resonant exchange qubits via circuit quantum electrodynamics, *Phys. Rev. B* **94**, 205421 (2016).
- [55] A. Warren, E. Barnes, and S. E. Economou, Long-distance entangling gates between quantum dot spins mediated by a superconducting resonator, *Phys. Rev. B* **100**, 161303(R) (2019).
- [56] M. Benito, J. R. Petta, and G. Burkard, Optimized cavity-mediated dispersive two-qubit gates between spin qubits, *Phys. Rev. B* **100**, 081412(R) (2019).
- [57] A. Warren, U. Güngördü, J. P. Kestner, E. Barnes, and S. E. Economou, Robust photon-mediated entangling gates between quantum dot spin qubits, *Phys. Rev. B* **104**, 115308 (2021).
- [58] S. M. Young, N. T. Jacobson, and J. R. Petta, Optimal control of a cavity-mediated iSWAP gate between silicon spin qubits, *Phys. Rev. Appl.* **18**, 064082 (2022).
- [59] S.-S. Gu, S. Kohler, Y.-Q. Xu, R. Wu, S.-L. Jiang, S.-K. Ye, T. Lin, B.-C. Wang, H.-O. Li, G. Cao *et al.*, Probing two driven double quantum dots strongly coupled to a cavity, *Phys. Rev. Lett.* **130**, 233602 (2023).
- [60] S. Yang, X. Wang, and S. D. Sarma, Generic Hubbard model description of semiconductor quantum-dot spin qubits, *Phys. Rev. B* **83**, 161301(R) (2011).
- [61] S. Das Sarma, X. Wang, and S. Yang, Hubbard model description of silicon spin qubits: Charge stability diagram and tunnel coupling in Si double quantum dots, *Phys. Rev. B* **83**, 235314 (2011).
- [62] J. R. Schrieffer and P. A. Wolff, Relation between the Anderson and Kondo Hamiltonians, *Phys. Rev.* **149**, 491 (1966).
- [63] L. H. Pedersen, N. M. Møller, and K. Mølmer, Fidelity of quantum operations, *Phys. Lett. A* **367**, 47 (2007).
- [64] K. Eng, T. D. Ladd, A. Smith, M. G. Borselli, A. A. Kiselev, B. H. Fong, K. S. Holabird, T. M. Hazard, B. Huang, P. W. Deelman *et al.*, Isotopically enhanced triple-quantum-dot qubit, *Sci. Adv.* **1**, e1500214 (2015).
- [65] M. D. Reed, B. M. Maune, R. W. Andrews, M. G. Borselli, K. Eng, M. P. Jura, A. A. Kiselev, T. D. Ladd, S. T. Merkel, I. Milosavljevic *et al.*, Reduced sensitivity to charge noise in semiconductor spin qubits via symmetric operation, *Phys. Rev. Lett.* **116**, 110402 (2016).
- [66] B. Bertrand, H. Flentje, S. Takada, M. Yamamoto, S. Tarucha, A. Ludwig, A. D. Wieck, C. Bäuerle, and T. Meunier, Quantum manipulation of two-electron spin states in isolated double quantum dots, *Phys. Rev. Lett.* **115**, 096801 (2015).
- [67] F. Martins, F. K. Malinowski, P. D. Nissen, E. Barnes, S. Fallahi, G. C. Gardner, M. J. Manfra, C. M. Marcus, and F. Kuemmeth, Noise suppression using symmetric exchange gates in spin qubits, *Phys. Rev. Lett.* **116**, 116801 (2016).
- [68] T. Meunier, V. Calado, and L. Vandersypen, Efficient controlled-phase gate for single-spin qubits in quantum dots, *Phys. Rev. B* **83**, 121403(R) (2011).
- [69] M. Russ, D. M. Zajac, A. J. Sigillito, F. Borjans, J. M. Taylor, J. R. Petta, and G. Burkard, High-fidelity quantum gates in Si/SiGe double quantum dots, *Phys. Rev. B* **97**, 085421 (2018).
- [70] D. C. McKay, C. J. Wood, S. Sheldon, J. M. Chow, and J. M. Gambetta, Efficient Z gates for quantum computing, *Phys. Rev. A* **96**, 022330 (2017).
- [71] J. M. Martinis and M. R. Geller, Fast adiabatic qubit gates using only σ_Z control, *Phys. Rev. A* **90**, 022307 (2014).

- [72] K. M. Prabhu, *Window Functions and Their Applications in Signal Processing* (Taylor & Francis, 2014).
- [73] V. W. Scarola, K. Park, and S. Das Sarma, Chirality in quantum computation with spin cluster qubits, *Phys. Rev. Lett.* **93**, 120503 (2004).
- [74] K. D. Petersson, J. R. Petta, H. Lu, and A. C. Gossard, Quantum coherence in a one-electron semiconductor charge qubit, *Phys. Rev. Lett.* **105**, 246804 (2010).
- [75] X. Mi, S. Kohler, and J. R. Petta, Landau-Zener interferometry of valley-orbit states in Si/SiGe double quantum dots, *Phys. Rev. B* **98**, 161404(R) (2018).
- [76] B. Paquelet Wuetz, D. Degli Esposti, A.-M. J. Zwerver, S. V. Amitonov, M. Botifoll, J. Arbiol, A. Sammak, L. M. Vandersypen, M. Russ, and G. Scappucci, Reducing charge noise in quantum dots by using thin silicon quantum wells, *Nat. Commun.* **14**, 1385 (2023).
- [77] F. Borjans, X. Zhang, X. Mi, G. Cheng, N. Yao, C. A. C. Jackson, L. F. Edge, and J. R. Petta, Probing the variation of the intervalley tunnel coupling in a silicon triple quantum dot, *PRX Quantum* **2**, 020309 (2021).
- [78] X. Wu, D. R. Ward, J. Prance, D. Kim, J. K. Gamble, R. Mohr, Z. Shi, D. Savage, M. Lagally, M. Friesen *et al.*, Two-axis control of a singlet-triplet qubit with an integrated micromagnet, *Proc. Natl. Acad. Sci. USA* **111**, 11938 (2014).
- [79] Z. Shi, C. B. Simmons, D. R. Ward, J. R. Prance, R. T. Mohr, T. S. Koh, J. K. Gamble, X. Wu, D. E. Savage, M. G. Lagally *et al.*, Coherent quantum oscillations and echo measurements of a Si charge qubit, *Phys. Rev. B* **88**, 075416 (2013).
- [80] D. M. Zajac, T. M. Hazard, X. Mi, E. Nielsen, and J. R. Petta, Scalable gate architecture for a one-dimensional array of semiconductor spin qubits, *Phys. Rev. Appl.* **6**, 054013 (2016).